Rapid transformation of biogenic silica to authigenic clay during reverse weathering

Simin Zhao[1#], Emily M. Saad[1#], Rebecca A. Pickering[2], Pan Liu[1], Hongyan Zuo[3], Linduo Zhao[4], Ellery Ingall[1], Martial Taillefert[1], Christopher T. Reinhard[1], Hailiang Dong[3], Jeffrey W. Krause[2,5]*, Yuanzhi Tang[1]*

[1]School of Earth and Atmospheric Sciences, Georgia Institute of Technology, Atlanta, GA 30332-0340, USA

[2]Stokes School Marine and Environmental Sciences, University of South Alabama, Mobile, AL 36688, USA

[3]Department of Geology & Environmental Earth Science, Miami University, Oxford, OH 45056, USA

[4] Illinois Sustainable Technology Center, University of Illinois Urbana-Champaign, Champaign, IL 61820, USA

[5]Dauphin Island Sea Lab, Dauphin Island, AL, 36528, USA

[#]Authors contributed equally.

*Corresponding authors: Yuanzhi Tang (yuanzhi.tang@eas.gatech.edu), Jeffrey W. Krause (jkrause@disl.edu)

This is a non-peer-reviewed preprint submitted to EarthArXiv. The manuscript has been submitted to Science Advances for peer review. Please note that the content may change after the peer-review. The finanal version of this mamuscript after acceptance will be available via the "Peer-reviewed publication DOI"

Abstract

Formation of authigenic clay minerals during early diagenesis of marine sediments, termed "reverse weathering" (RW), is an important process for regulating ocean pH and atmospheric CO_2 over geologic time scales. It is also considered a"missing sink" of the modern marine Si cycle. Although the importance of RW has been increasingly recognized, the rate and mechanisms of this process remain elusive. This study investigated the mechanisms, kinetics, and mineral products derived from diatom biogenic silica in RW. We show the formation of annite (Fe(II)-rich mica) in 40 days, the most rapid process observed to date and the first specific mineral phase identified for RW. Unraveling the kinetics and mechanisms of secondary phase formation suggests an up to one order of magnitude upward revision of potential RW reaction rates in marine sediments. This implies that RW is far more responsive to changes in ocean chemistry and climate state than previously envisioned, suggesting a major role for RW in regulating Earth's carbon and alkalinity cycles in the modern ocean, through Earth's history.

Keywords: reverse weathering, authigenic clay formation, silica sink, carbon cycle, marine trace element cycle

Reverse weathering in marine sediments, proposed in the 1960s (*1-4*), was suggested to be a major component of the missing burial sinks of silicon (Si) and alkalinity (HCO_3^-) produced during terrestrial weathering. It follows the general reaction of:

$$\text{biogenic silica} + Al(OH)_4^- + (Fe^{2+}, Fe^{3+}, Mg^{2+}, K^+, Li^+) + HCO_3^- \rightarrow \text{aluminosilicate minerals} + CO_2 + H_2O \quad \text{(Eq. 1)}$$

Through the reaction, amorphous biogenic silica (e.g., diatom silica originating from the upper water column or surface-lit sediments; hereafter bSi) transforms into authigenic aluminosilicates (*5*), consuming cations (e.g., Fe, Mg, K, Li) and alkalinity (HCO_3^-) while producing CO_2. CO_2 production during reverse weathering has been suggested to affect ocean pH and global climate over geological time and is incorporated into biogeochemical models tracing climate evolution in Earth's history (*1, 6-8*). These processes are only beginning to be considered in elemental budgets and biogeochemical cycle models (*9*). For instance, the marine Si budget has been long observed to be out of balance with burial fluxes insufficient to match inputs (*10*). Recent studies estimated that the Si burial flux due to marine reverse weathering is 4.5–4.9 Tmoles Si/year (*11, 12*), which potentially balances the marine Si deficit. These recent estimates make reverse weathering the second largest sink among all currently recognized output processes within the global marine Si budget (*12*). Upward revision of the magnitude of marine reverse weathering in the global Si budgets has significant implications for the associated carbon cycle (e.g., seawater alkalinity), coastal acidification, sequestration of other elements (e.g., Fe, Al, Mg, K), and direct and indirect feedbacks on marine primary productivity, global climate (*10, 12, 13*), and anthropogenic interventions of the carbon cycle for geoengineered climate solutions (*14, 15*).

Understanding of reverse weathering in marine systems has improved in the past several decades, with seminal studies demonstrating the effectiveness of RW for transforming bSi and the

63 possibility of rapid clay mineral formation during RW, in contrast to previous frameworks in which
64 RW was neglected or thought to occur on the order of 10^3–10^6 years (*16*). These studies relied on
65 indirect evidence from field observations to indicate rapid Si and Al reactions, e.g., stoichiometric
66 relationships between dissolved Al and Si in sediment pore waters (*17-19*). Strong associations of
67 bSi with authigenic clay minerals and cation-rich aluminosilicate coatings on diatom frustules in
68 deep-sea and deltaic sediments implied the importance of diatoms in this process (*16, 20, 21*), with
69 subsequent Si stable isotope measurements providing evidence for the connection between
70 sediment bSi with authigenic clay mineral formation (*22*). Direct evidence of reverse weathering
71 has also been obtained through experimental incubation of bSi with sediments (*5, 9, 23*), which
72 shows bSi alteration and formation of authigenic K- and Fe-rich mica- or smectite-like clays after
73 10–36 months (*5, 9, 23*).

74 However, despite these advances significant uncertainty remains around the controlling
75 geochemical factors, kinetics, mechanisms, and specific reaction products of reverse weathering.
76 First, the function of potential reactant species and the phases of reaction products are poorly
77 constrained. Despite the commonly observed association between Fe and aluminosilicate phases
78 (*9*), the roles of Fe- and Al-containing species in the transformation process remain elusive. The
79 authigenic clay phases produced from reverse weathering are small particles (*24*), making their
80 characterization and detection highly challenging using traditional techniques (*25, 26*).
81 Characterization of authigenic clays in field samples is further confounded due to the mixing with
82 abundant detrital clays (*27*). Identification of such authigenic products has previously relied on lab
83 incubations, usually based on compositions from extraction methods and scanning electron
84 microscopy with energy dispersive spectroscopy (SEM-EDX) (*21, 28*), and the comprehensive
85 mineral identifications were challenging or lacking (*21*). Second, previous lab incubations, which

ranged in duration from 10 to 36 months (*5, 21, 29*) only examined the reaction products at the end point. Thus, the time-course dynamics are almost entirely unknown. Third, specific reaction mechanisms are poorly constrained. Although authigenic clay diagenesis is thought to involve dissolution and reprecipitation reactions, with the participation of Al, Si, and cations (e.g., Mg and Fe, Eq. 1) (*9, 23*), the roles of specific elements and their speciation (e.g., oxidation state, dissolved vs solid phase) remain unclear.

To improve mechanistic understanding of the reverse weathering processes, controlled laboratory experiments were conducted using diatom bSi under representative marine dissolved Fe(II) concentrations and combinations of Fe- and Al-hydroxide minerals (hereafter Fe/Al minerals). Experiments were conducted in anoxic conditions using custom-built two-chamber reactors, which separate bSi from Fe/Al minerals by a dialysis membrane (Figure S1). This reactor design allows for the mixing solely of dissolved species (e.g., Si, Fe, and Al) and separates the transformed bSi by reverse weathering from the Fe/Al mineral phases to facilitate systematic characterization. All experiments were initially amended with 150 μM dissolved silicic acid ($Si(OH)_4$, denoted as DSi) to mimic field-observed pore water $Si(OH)_4$ concentration (*23, 28, 30*). Experimental groups with and without bSi substrate were included. Both groups were incubated with dissolved Fe(II) concentrations of 0, 100, or 1000 μM, with or without Fe and/or Al minerals (denoted as Fe, Al, or FeAl). Group I (with bSi) was used to constrain the dissolution and re-precipitation processes and phase change of bSi. Group II (without bSi) was used to interpret the $Si(OH)_4$ precipitation mechanism observed in Group I. Table 1 and Table S1 summarize treatment conditions and sample labels. Duplicate treatments were run for all 24 combinations. With this experimental matrix, we directly elucidated the reaction mechanisms and the roles of Fe and Al and their associated mineral phases in authigenic clay formation, constrained the reaction rates,

and revealed the specific authigenic mineral phases formed.

Results

Rapid authigenic clay formation after one month of incubation

SEM analyses after 40 days of incubation showed significant transformation of bSi in the presence of 1000 μM Fe(II) (Figure 1B), as compared to no obvious morphological transformation in the absence of Fe(II) (Figure 1A). Energy dispersive X-ray spectroscopy (EDX) analyses (Figure 1B) showed Fe, Si, and O distributions overlapping with bSi, suggesting Fe precipitation on and/or incorporation into bSi frustules, consistent with earlier observations (*9, 31*). In the presence of both 1000 μM Fe(II) and Al mineral, bSi was extensively altered and showed distinct morphological features (Figure 1C). The overlapping of Fe and Al EDX maps (Figure 1C) indicated Fe and Al precipitation on and/or incorporation into bSi (*9, 31*). In addition, aggregated flaky precipitates rich in Fe, Si, Al, and Mg were observed on bSi for 1000Fe (II)+bSi+Al (Figure 1D) and 1000 Fe (II)+bSi+FeAl treatments (Figure 1E), suggesting the formation of authigenic clay phases. EDX maps of individual new phases without the visual presence of nearby/underlying bSi residue (i.e., near complete transformation of bSi) also showed an overlapping composition of Si with Fe and Al (Figure S2). For bSi treated with 100 μM Fe(II) and minerals, SEM analysis showed a lower alteration extent for bSi, and no obvious layered phases could be discerned.

Experimental groups in the 1000 μM Fe(II) treatments showing signs of secondary mineral formation under SEM were further analyzed by synchrotron X-ray diffraction (XRD) and high-resolution transmission electron microscopy (HRTEM) for phase identification. Harvested solids from the bSi chamber of the 1000Fe(II)+bSi+Al treatment showed the appearance of a new broad diffraction peak at ~7.8 Å (Figure 2A), suggesting the formation of clay phase(s) with large

interlayer spacing. The broadening of this peak is likely due to small particle size and/or poor crystallinity (*32*). New peaks in the d_{060} region were also observed for 1000Fe(II)+bSi+Al and 1000Fe(II) bSi+FeAl at 1.57 and 1.54 Å, respectively (Figure 2B), indicating the formation of trioctahedral smectite clays (*32, 33*). HRTEM analyses were further conducted on the harvested solids from bSi chamber of 1000Fe(II)+bSi+Al treatment and confirmed the formation of a clay phase (Figure 3A). Specifically, EDX spectrum showed the new phase to be mainly composed of Fe, Mg, Al, K, and Si. Selected area electron diffraction (SAED) analysis showed the presence of six d-spacings at 0.45, 0.26, 0.22, 0.17, 0.15, and 0.12 nm, typical of phyllosilicates (*34*). Based on the combined EDX composition (K-rich Fe-Al-Si phase) and SAED patterns, the new clay mineral phase is best identified as annite, an Fe(II)-rich phyllosilicate mineral in the mica group (Figure 3A). Additionally, porous morphological features of diatom bSi were observed (Figure 3A), confirming clay growth on bSi. In comparison, the no-mineral control of the 1000 μM Fe(II) treatment (1000Fe(II)+bSi) showed only altered bSi and Fe/Mg/Ca/Si-rich phases without evidence of crystallization (Figure 3B), consistent with SEM-EDX observation (Figure 1B).

Authigenic clay formation mechanism revealed by solution phase evolution

The transformation of bSi to clay observed in this study is further supported by the time evolution of dissolved $Si(OH)_4$ and Fe(II) (Figure 4), which demonstrates the complex interactions between the dissolution of solid phases (bSi, Fe mineral, Al mineral) and the consumption of dissolved phases ($Si(OH)_4$, Fe(II), Al) through processes such as sorption and reprecipitation. Thus, we define the observed dissolved $Si(OH)_4$ concentration, $[Si(OH)_4]$, as the apparent dissolution of bSi, which is the net result of bSi dissolution and consumption.

In the presence of bSi and no Fe(II), $[Si(OH)_4]$ reached 1039 μM in 40 days (bSi; Figure

155 4B), consistent with the thermodynamically predicted solubility of amorphous silica under the
156 experimental conditions (*35*) and observations of asymptotic [$Si(OH)_4$] in marine sediment
157 porewaters (*36, 37*). Treatments containing Al mineral significantly reduced [$Si(OH)_4$] at steady
158 state (Figure 4B). Specifically, the presence of Al mineral (bSi+Al) and Fe+Al minerals (bSi+FeAl)
159 decreased [$Si(OH)_4$] by 16% and 28%, respectively. The presence of Fe mineral (bSi+Fe) showed
160 less influence, with only 9% decrease in [$Si(OH)_4$] compared to the no-mineral control (bSi)
161 (Figure 4B).

162 In the presence of bSi and Fe(II), the concentrations of Fe(II) and $Si(OH)_4$ at steady state
163 both decreased. For 100 μM Fe(II) treatments, all Fe(II) was removed from solution within ~20
164 days (Figure 4C), consistent with the thermodynamic prediction that the system was oversaturated
165 with respect to Fe(II)-silicate phases (*35*) and likely involved Fe(II) precipitation. For 1000 μM
166 Fe(II) treatments, all reactions showed significant but not complete Fe(II) removal (Figure 4E).
167 The addition of Fe and Al minerals showed no systematic effects on Fe(II) removal in the 100 μM
168 and 1000 μM Fe(II) treatments (Figures 4C and E, S3A). For 100 μM Fe(II) treatments, the steady
169 state [$Si(OH)_4$] in the no-mineral control (bSi) decreased to 904±54 μM (Figure 4D). The presence
170 of minerals further decreased steady state [$Si(OH)_4$] value, i.e., bSi+Al at 620±50 μM, bSi+FeAl
171 at 596 ±27 μM, and bSi+Fe at 756±19 μM (Figure 4D). A similar inhibition effect by dissolved
172 Fe(II) was observed in 1000 μM Fe(II) treatments, with all the 1000 μM Fe(II) treatments (Figure
173 4F) showing lower [$Si(OH)_4$] than their corresponding samples of no Fe(II) (Figure 4B) and 100
174 μM Fe(II) treatments (Figure 1D). Specifically, steady state [$Si(OH)_4$] for the no-mineral control
175 (bSi) decreased by 36% to 668±75 μM in the presence of 1000 μM Fe(II) (Figure 1F), compared
176 to the no Fe(II) treatment (Figure 4B). The Al mineral treatment (bSi+Al) further decreased
177 [$Si(OH)_4$], whereas Fe mineral treatment (bSi+Fe) showed less of an effect on [$Si(OH)_4$] (Figure

4F). Relative to the corresponding no Fe(II) groups, steady state [$Si(OH)_4$] in the 1000 μM Fe(II) groups decreased by 43%, 54%, and 31% for the Al mineral (bSi+Al), Fe+Al mineral (bSi+FeAl), and Fe mineral (bSi+Fe) treatments, respectively. The initial rate of apparent silica dissolution was calculated by fitting a linear regression to the apparent [$Si(OH)_4$] profile during the first ~7 days. Compared to the bSi-only control, the initial rates of apparent silica dissolution were reduced by the presence of Fe(II) and Al/Fe minerals (Figure S3B).

In the 150 μM $Si(OH)_4$ treatments with no added bSi (experimental treatments DSi), the presence of Al mineral and dissolved Fe(II) accelerated $Si(OH)_4$ consumption (Figure S4B, D and F) likely due to precipitation. In the absence of Fe(II) or Fe/Al minerals, [$Si(OH)_4$] in the DSi treatment persisted at 150 μM throughout the experiment but was reduced in the presence of Al mineral (+Al) and Fe+Al mineral (+FeAl) treatments, respectively (Figure S4B). In the presence of Fe(II), [$Si(OH)_4$] was further consumed (Figure S4D and F). In the 100 μM (Figure S4D) and 1000 μM Fe(II) DSi treatments (Figure S4F), [$Si(OH)_4$] was reduced to 94±5 μM and 96±0 μM at steady state, respectively; and the addition of Fe+Al mineral (+FeAl), Fe mineral (+Fe), or Al mineral (+Al) further reduced [$Si(OH)_4$]. The consumption of [$Si(OH)_4$] was accompanied by a decrease of Fe(II) (Figure S4C, E) and dissolved Al (discussed below), suggesting the precipitation of Si in the DSi treatments by Fe(II) and Al.

Dissolved Al concentrations in 0 μM Fe(II) treatments, with and without bSi, showed no trends over time except for occasional oscillations (Figure S5A), likely due to the difference in dissolution and precipitation rates. The 100 and 1000 μM Fe(II) treatment groups, with or without the presence of bSi, also showed occasional spikes of dissolved Al (Figure S5B and S5C) but at smaller amplitude than the 0 μM Fe(II) treatment. Additionally, in the control experiment containing only 100 μM Fe(II), 30 μM dissolved Al, and 150 μM $Si(OH)_4$ ("dissolved only"), Al

was completely removed from solution within 1 day (Figure S4B), consistent with thermodynamically predicted oversaturation with respect to Fe(II)-silicates, Al-silicates, and amorphous Al-minerals under these conditions (*35*).

Discussion

With the observed formation of annite after 40-day incubation in the presence of Fe(II), Al mineral, and dissolved [$Si(OH)_4$], below we further interpret the formation mechanism from both the source and sink perspectives (Figure 5A), reveal the authigenic clay products and formation timescale, and discuss the implications for the coupled carbon-silicon (C-Si) cycle (Figure 5B).

Authigenic clay formation mechanism

Sources: Fe and Al sources

We tested Fe and Al phases as key reactants in reverse weathering, which has been suggested by multiple field studies (*23, 29, 31*) but for which direct evidence and mechanistic understanding have been lacking. The Fe sources (Fe(II) and Fe(III)-mineral) used in this study are representative of Fe(II) produced in marine sediments by biotic/abiotic reductive dissolution of Fe minerals and Fe(III)-bearing Fe oxyhydroxides ($Fe(OH)_3$) (*23, 29, 31, 38*). In marine sediments, the source of Al mainly comes from the dissolution of Al flocs and Al minerals (such as Al oxyhydroxide and clay minerals). Dissolved Al concentrations in marine sediments are typically very low. i.e., nanomolar level (*17*). However, as local, transient production of dissolved Al (via the aforementioned dissolution pathways) occurs, it would lead to the rapid precipitation of secondary minerals as observed in this study. There are many potential mineral phases that could supply dissolved Al and Fe to sediment pore waters. For this study, common Fe- and Al-

224 containing phases were chosen to illustrate the process and the potential influence of such phases
225 on reverse weathering.
226
227 ***Apparent bSi dissolution***
228 Reverse weathering reactions during early diagenesis require a Si source. The efficiency
229 of bSi recycling can be a constraint, e.g., lower efficiency in colder temperatures (*39, 40*). While
230 sediment bSi can include microplankton (e.g., diatoms and Rhizaria (*21*)) and siliceous sponge
231 spicules (*41*), diatoms predominate modern bSi production (*12, 42, 43*). In this study, we observed
232 a decrease in apparent bSi dissolution (quantified as reduced asymptotic $[Si(OH)_4]$) in the presence
233 of dissolved Fe(II) and Fe/Al-containing minerals, consistent with the inferences from previous
234 studies (discussed below). The influence of Al on bSi dissolution was evident in the Al mineral
235 treatments regardless of Fe(II) concentration, which resulted in lower initial rates of apparent silica
236 dissolution (Figure S3B) and final dissolution extent (Figure 4). A similar effect was observed
237 with Fe(II), where the magnitude of the effect increased with increasing Fe(II) concentration from
238 100 to 1000 μM. However, Fe mineral treatments showed less suppression of apparent bSi
239 dissolution. The decreased $[Si(OH)_4]$ in the presence of dissolved Fe(II), Al mineral, or Fe+Al
240 mineral (~300-700 μM $Si(OH)_4$ equilibrium concentration) (Figure 4B, D, F) are close to pore
241 water $[Si(OH)_4]$ reported for deltaic and oceanic sediments (*31*). Additionally, in the absence of
242 bSi, Al mineral and Fe(II) exerted the strongest control over $[Si(OH)_4]$ precipitation (Figure S4B,
243 D, and F).
244 The decrease in steady-state $[Si(OH)_4]$ mimics the inverse relationship between pore water
245 $[Si(OH)_4]$ and the ratio of lithogenic minerals to bSi in marine sediments (*44*), where lithogenic
246 phases affect the $Si(OH)_4$ thermodynamic equilibrium (*31*). Such a $[Si(OH)_4]$ decrease in

sediments has been previously suggested to result from absorption (*45*) or incorporation of dissolved ions into bSi resulting in reduced bSi dissolution (*9*). Over the 40-day experiment, our results showed that when Fe(II) was 1000 μM, the observed bSi alteration product was enriched in Fe (Figures 1 and 3) and slightly enriched in Ca and Mg (Figure 3). Such cation incorporation processes likely contributed to the observed decrease in bSi dissolution compared to the no Fe(II) treatment. Compared to Fe(II), the Fe mineral treatment did not suppress bSi dissolution to the same degree (Figure 4B, D, F). This may reflect that Fe(III) incorporation in bSi is less favorable (*46*), consistent with the idea that dissolved Fe(II), as opposed to Fe(III), can suppress the dissolution rate of bSi (*46*). Al incorporation into bSi has also been shown to reduce its solubility (*47, 48*), as prior work showed lower bSi dissolution extent with higher diatom frustule Al/Si ratios (*39*). Based on the observed Al association with the altered bSi phase in the Al mineral treatment (Figures 1 and 4), our results further demonstrate rapid Al-induced inhibition of bSi dissolution. At the experimental pH of 7.5 used in this study, the bSi surface is negatively charged (*45*), which should readily absorb dissolved cations, such as Fe(II) and Al(III). The strong structural association of Fe and Al with bSi (Figures 2 and 4) further supports the inhibition of bSi dissolution due to the incorporation of these elements.

The dissolution of bSi, and subsequent build-up of [$Si(OH)_4$] in marine sediments, is further governed by the interplay between Si release and removal mechanisms. Authigenic mineral formation (i.e., reverse weathering) has been proposed to explain the decreases in porewater [$Si(OH)_4$] relative to apparent saturation (*1, 31, 44, 45*). Our study showed that in the absence of bSi, [$Si(OH)_4$] dramatically decreased in the presence of Al mineral and/or dissolved Fe(II) (Figure S4B, D, F). At the studied pH of 7.5, removal of $Si(OH)_4$ by the Al mineral can result from adsorption of $Si(OH)_4$ to the positively charged $Al(OH)_3$ (*49*) and/or co-precipitation of dissolved

Al and $Si(OH)_4$. The presence of Fe(II) could have triggered the coprecipitation of Fe(II) and $Si(OH)_4$, explaining the overall lower extent of bSi apparent dissolution as compared to no-Fe(II) treatments. In the presence of bSi, Si sequestration by authigenic mineral formation was observed. The Fe(II) and Al mineral treatments (bSi+Al) were among those with the lowest apparent soluble [$Si(OH)_4$] (496±20 μM for 1000 μM Fe(II) treatment, Figure 4F), and the newly formed precipitates were identified as Si-rich clay (Figure 3). Overall, our results provide clear evidence of rapid $Si(OH)_4$ sequestration by authigenic mineral formation, which is likely a dominant mechanism for decreased [$Si(OH)_4$] in marine sediment pore waters.

Sinks: The reprecipitation of $Si(OH)_4$ to form authigenic clay minerals

Although authigenic clay mineral formation has been commonly recognized to involve dissolution and reprecipitation processes with the participation of Al, Si, and cations (e.g., Mg and Fe) (*9, 23*), direct evidence for such a clay mineral formation mechanism is lacking. Our results showed that the dissolution of bSi and input of dissolved Fe(II) and Al was followed by the re-precipitation of $Si(OH)_4$ to form an authigenic annite on bSi. As discussed above, dissolved Fe(II), Al, and $Si(OH)_4$ are sources for authigenic clay formation. SEM and TEM observations (Figures 1 and 3) of the new phase formed in bSi-containing experimental chamber showed porous bSi frustule fragments and the associated new annite phase, supporting the precipitation of clay on bSi. This precipitation outcome is consistent with a previously proposed diagenetic pathway involving frustule alteration and conversion to authigenic clay (*21, 28*). The precipitation of dissolved Si, Al, and Fe(II) is also supported by the precipitation in the DSi experiment (Figure S3A−F) triggered by Fe(II) and Al.

Despite the previously acknowledged importance of Fe in reverse weathering (*5, 9, 23*),

293 the role of Fe concentration and speciation [i.e., Fe(II) vs Fe(III)] has remained elusive.
294 Michalopoulos and Aller (1995) directly observed the transformation of sand and FeOOH-coated
295 sand to a Fe-K-rich phase. Subsequent studies also found authigenic phases from altered bSi to be
296 Fe-rich (Michalopoulos et al., 2000). Soluble Fe(II) has been suggested to be more favorable for
297 early diagenesis due to its higher mobility (*31*). Michalopoulos and Aller (1995) assumed that Fe
298 in the Fe-K-rich mineral was primarily Fe(II) as the dissolved [Fe(II)] concentration was high in
299 the anoxic Amazon shelf sediment they used for the experiment. Loucaides et al. (2010) observed
300 Fe association with diatom frustules incubated with field sediments, but not in their laboratory-
301 incubated diatom frustules. These authors attributed this discrepancy to oxic laboratory conditions
302 (*9*) which resulted in the formation of Fe(III) oxyhydroxides, while the more reducing natural
303 conditions resulted in Fe(II) incorporation into diatom frustule. Here we show the formation of the
304 new clay mineral phase even without the presence of the Fe(III)-mineral $Fe(OH)_3$ (Figure 2). This
305 suggests that Fe(III) minerals do not play a significant role in rapid authigenic clay mineral
306 formation. Instead, the presence of soluble Fe(II) exerted a significant role in inducing Si
307 precipitation (Figures 1 and S3). Thus, we infer that under our experimental conditions, Fe(II),
308 rather than Fe(III)-minerals, was a major control on rapid authigenic clay formation.

309 Previous lab incubations and field studies found a strong association of Al with bSi as
310 authigenic precipitates (*9*). The role of Al in inducing precipitation is supported by our results, as
311 the 1000Fe(II)+bSi+Al treatment showed annite formation while the 1000Fe(II)+bSi treatment
312 showed no authigenic clay formation in the same time frame. The precipitation of $Si(OH)_4$ by Al
313 is also supported in the incubation of DSi (Figure S3B, D, and F), in which the presence of Al
314 mineral resulted in the highest consumption of $Si(OH)_4$, likely via adsorption and coprecipitation.
315 The experimental apparatus ensured that the newly formed Fe-Al-Si (annite) phase (Figure 2 and

316 3) in the bSi-containing chamber could only result from the diffusion of dissolved Al through the
317 membrane from the Al mineral-containing chamber (Figure S1). Though the dissolved Al
318 dynamics were only partially captured (Figure S4), these data suggest that the dissolution and
319 reprecipitation reactions were rapid, and not resolved by our sample interval of 2–7 days.

320 Our results highlight the roles of Fe(II) and Al in triggering $Si(OH)_4$ precipitation and
321 authigenic clay formation. They also provide direct evidence for previously proposed mechanisms
322 and recent field observations of the coupled Fe and Al cycles with Si and authigenic clay formation
323 in deltaic environments (*23, 31, 50*). Although we identified the participation of other cations (Mg,
324 K, and Ca) in the authigenic phase formation, these cations did not appear to play driving roles
325 under our experimental conditions (artificial seawater at pH 7.5). However, in marine settings with
326 fluctuations of local cation concentrations, pH, and salinity, these cations might be a factor in
327 authigenic clay formation. For example, the observed Mg-smectite formation in saline
328 environments with pH higher than 8.2 (*51*) might suggest the potential roles of pH and salinity in
329 controlling the participation of other cations in this process (*51, 52*).
330
331 **Products and time scale of authigenic clay formation**

332 Through controlled laboratory incubations and physical isolation of bSi from other mineral
333 reactants (Figure S1) we were able to characterize the initial clay mineral product of reverse
334 weathering processes. Robust identification of clay type is difficult as common Fe-rich clays have
335 similar structures and chemical compositions. For example, Fe-smectites, Fe-bearing illite, and
336 Fe-muscovite have similar structures and only slight variations in chemical composition. They can
337 also transform into each other during diagenesis (e.g., mica to smectite and illite, smectite to illite)
338 and/or form mixed-layer phases (*32, 53, 54*). By combining the SAED diffraction patterns and

EDX-derived chemical compositions, we identified the experimentally-derived clay product to be annite, an Fe(II)-rich phyllosilicate phase in the mica group (Figure 4), which is consistent with the proposed mica-type mineral products in field incubations of FeOOH-coated quartz by Michalopoulos and Aller (1995). To our knowledge, this is the first direct identification of a specific authigenic clay phase formed during early diagenetic reverse weathering reactions.

The timescale of authigenic annite formation (~40 days) observed here was considerably shorter than previously observed timescales (10–36 months) (*5, 9, 23*). Although the abiotic experiment here applied organic-coating-removed diatoms to mimic coating removal in natural conditions, such removal is not expected to cause divergent rate from natural settings for the following two reasons. First, organic coating removal by natural heterotrophic bacteria can occur quickly (e.g., <2 weeks) and bacteria-mediated Si generation is similar though not as rapid as that of organic coating-removed frustules by acid-cleaning.(*55*). Second, the optimized low-temperature plasma-ashing coating-removing approach applied in this study can sustain both SiO_2 structure and high specific surface area (*56*) such that the dissolution rate of plasma-ashed bSi is close to that of raw bSi. The dissolution rate of plasma-ashed bSi is one magnitude lower than that derived from conventional harsh cleaning methods (e.g., nitric acid, hydrochloric acid, peroxide, and/or baking. Note, the short time scales of ~40 days for the reverse weathering process in this study, is significantly longer than the mixing time of < 40 hours (Figure S6) across the dialysis membrane of the experimental reactor (Figure S1). Time-course data reported here provide insights on the factors affecting the rate of early diagenesis. As discussed above, both dissolution and reprecipitation exert roles in the diagenetic timeline. bSi dissolution affects the Si source for precipitation and the concentration stabilized after 30–40 days (Figure 4). Previous studies have shown that the bSi dissolution rate is mainly affected by the surface area and charge of different

diatom species (*45*). Although our study only used one diatom species as a representative bSi source, its surface area (~50 m^2/g) is typical of diverse diatom species (*57*), but a factor of 3–6 lower than other biosiliceous structures which may be allochthonous in marine coastal systems (e.g., phytoliths, (*58*)). As for the controlling factor in Al mineral dissolution, $Al(OH)_3$ dissolution was estimated to be shorter than our sampling interval (2–7 days) (Figure S4). In terms of precipitation, the effects of mineral substrates (e.g., bSi or other mineral phases in natural sediments) may also affect the diagenetic timescale. Taken together, these results provide a basis to further constrain the potential rates and Si sinks via authigenic clay formation in marine sedimentary environments.

Implications for reverse weathering rates, the sedimentary Si sink, and the global carbon cycle

The reaction time scale, rate, and associated Si sink of reverse weathering have been consistently revised upwards since the process was added to marine Si budgets in the early 2000s (*59*). The two milestone revisions updated the timescale of reverse weathering from thousands of years (*16*) to 20–36 months (*5*, *23*) and then to 10 months (*21*, *29*), which is in line with the upward revision of reverse weathering as a global Si sink from 0 to 1.5 T mole/yr to 4.5–4.9 T mole/yr (*10*, *11*). The reverse weathering rates extrapolated from these budgets were also updated to 1.3×10^{-6} $\mu mol/cm^3/s$ (*21*) and 3.9×10^{-6} $\mu mol/cm^3/s$ (*11*, *60*).

In this study, we demonstrated the rapid formation of annite (an Fe-rich mica) within 40 days. While it is important to acknowledge the challenges inherent in scaling rates derived under laboratory conditions to rates expected in the field, this is a required first step towards better constraining the rates and mechanisms of RW in marine sediments. We first apply a conventional

385 simplified zero-order reaction rate law (*21*) to the lab-derived rates, then scale to field rates via
386 bSi-to-sediment weight-to-weight ratio (Methods Section 2.2), assuming bSi weight percent in
387 sediments and average deltaic sediment density and porosity. This results in a $Si(OH)_4$ reaction
388 rate of 19.8×10^{-6} μmol/cm^3/s.

389 The rates extrapolated from our experiments are five times higher than the most recently
390 updated reverse weathering rate of 3.9×10^{-6} μmol/cm^3/s (*8, 11, 60*) (Table S3). This elevated rate
391 is particularly likely to be observed in regional areas like deltaic environments, which the
392 incubation conditions of this study are meant to closely mirror. We acknowledge that such
393 extrapolation may yield the upper boundary of the regional reverse weathering rate, as the reaction
394 conditions in the field may limit rates relative to laboratory conditions. In particular, natural
395 conditions that may lower reaction rates include lower reactant concentrations (Fe^{2+}, $Al(OH)_4^-$,
396 dissolved $Si(OH)_4$, and other dissolved cations) and reaction pH. On the other hand, however, field
397 rates can be accelerated by catalyzed authigenic mineral formation by preexisting substrates (*61,*
398 *62*) or through microbial activity (*63-65*), although direct evidence for the latter is missing for
399 conditions described in this experiment. A recent study utilizing sediment isotopic data combined
400 with reactive transport modeling similarly reported locally high rates of RW across the Peruvian
401 margin in response to local weather conditions (*66*). This present study provides the first direct
402 evidence to reveal the rapid occurrence of reverse weathering at one month. Therefore, we
403 conservatively suggest that rates of reverse weathering rate have the potential to be an order of
404 magnitude higher than presently thought, at least locally, indicating that reverse weathering
405 reactions are more responsive than previously recognized.

406 The results also have profound implications on the coupled C-Si cycles that modulate Earth's
407 climate. By applying the stoichiometries of alkalinity to Si couplings (Alk/Si ratio), the CO_2

release coupled with reverse weathering can be estimated from the Si budget to constrain CO_2 budgets as previously demonstrated with Earth system models (*6, 7*) (Supplementary Information Section S1). The reverse weathering CO_2 release in recently reported global carbon cycle budget by Isson et al., (*7*) was updated based on the updated reverse weathering rates (3.9×10^{-6} μmol/cm^3/s) and corresponding Si budget (4.5–4.9 T mole/yr) by Rahman et al (*11, 60*) (Table S4). This led to a revision in the contribution of reverse weathering to CO_2 release from 0.5 to 10 Tmole/yr CO_2 (*7*) (Supplementary Information Section S1, Table S4). In light of the RW more rapid rates extrapolated in this study, re-evaluating the more robust roles of RW in modulating the Si-C fluxes will be critical to constructing the global Si-C models.

The rates reported by this study suggest that RW could be a much stronger transient modulator of global carbon and alkalinity cycling in Earth's history and by future anthropogenic perturbations than currently appreciated. RW were thought to play less significant roles for the global carbon and alkalinity cycling since the start of Cambrian around 550 million years ago due to the previously assumed lower rates resulting from the proliferation of Si-biomineralizing organisms and lowered dissolved silica content in the ocean (*42, 67*). This conceptual view has been challenged by recent findings that the Permian to Early Triassic warming is likely relevant to an enhanced reverse weathering regardless of Si uptake by Si-biomineralizing radiolarians and sponges (*67-69*). Our results further support this recent view by showing that silica in the form of diatom-derived bSi does not necessarily result in previously assumed low/ineffective reverse weathering rates. Instead, the rapid modern reverse weathering rates derived from diatom-derived bSi provide a mechanistic basis to support the expansion of the significance of reverse weathering in potentially modulating of global carbon and alkalinity cycling in a more robust manner across geological time scales and to different Si-biomineralization species (e.g., radiolarians, sponges,

diatoms, allochthonous grasses, etc.). On the other hand, it is important to consider the robustness of RW when evaluating anthropogenic interventions such as coastal enhanced rock weathering for climate mitigation. There appears to be a strong capacity (i.e. the increased reverse weathering rate) to consume sedimentary Si in marine sediments by this process; thus, geoengineering strategies (e.g. olivine dissolution (*14, 15*)) which propose CO_2 sequestration via silicate mineral weathering may have lower net drawdown in CO_2 if reverse weathering reactions can quickly consume the mineral-liberated Si and move CO_2 back into the system. Therefore, the net efficiency factor of such geoengineering climate solutions, along with the necessary adjustments, must be further modeled and constructed.

Conclusions

This study demonstrated the rapid transformation of diatom-derived bSi and the formation of authigenic clay (annite, Fe-rich mica) within 40 days in the presence of Fe(II) and Al- and Fe-containing mineral phases. Specifically, dissolved Fe(II) and Al were identified as the primary drivers of reverse weathering under the experimental conditions of this study. A dissolution-reprecipitation mechanism for bSi transformation is further elucidated. This first mechanistic framework of rapid bSi transformation to authigenic clay highlights that RW can occurs monthly compared annually as previously reported. The results indicate an up to one order of magnitude upward revision of the reverse weathering reaction rates. This implies that RW is far more responsive to changes in ocean chemistry and climate state than previously envisioned, suggesting a major role for RW in regulating Earth's carbon and alkalinity cycles in the modern ocean and through Earth's history.

Materials and Methods

1. Materials, experiments, and analyses

1.1. Solid phase preparation and characterization

Two representative Fe- and Al-containing minerals, ferrihydrite ($Fe(OH)_3$) and amorphous Al hydroxide ($Al(OH)_3$), respectively, were synthesized following previous procedures (*70, 71*). The marine diatom *Thalassiosira pseudonana* was used as a bSi source (Reed Mariculture Inc.) and stored at -20 °C. Prior to use, biomass was thawed and repeatedly rinsed with deionized (DI) water (18 MΩ cm) to remove residual growth media. Rinsing started with the suspension of ~1 g of wet biomass in 50 mL of DI, followed by repeated shaking and centrifugation (2200 × g, 5 min) until the conductivity of the supernatant was constant and similar to that of DI water (< 20 μS cm^{-1}). The rinsed material was freeze-dried and gently ground. Then 0.2 g of the solid was placed in glass petri dishes for organic matter removal by low temperature plasma ashing (Plasma-Therm RIE) for 7 h at 350 W, 25 °C, and an O_2 flow rate of 60 standard cubic centimeters per minute (sccm), following our previous procedure (*56*). Compared to other common cleaning methods, our recent study showed that low temperature plasma ashing preserves the degree of structural order of the SiO_2 framework, efficiently removes organic carbon, and is the least impactful on frustule dissolution compared to other cleaning methods such as high temperature and/or harsh chemical treatments (*56*).

The structures of $Fe(OH)_3$, $Al(OH)_3$, and bSi were characterized by XRD, (PANalytical Empyrean, Cu Kα source). All three solid phases were confirmed to be X-ray amorphous (Figure S7). Organic carbon content of the plasma-cleaned bSi is 1.0 ± 0.09 wt%, measured by combustion using a CHNSO analyzer (Costech Instruments) after acid fuming over night (*72*). A portion of the cleaned bSi was digested (0.2 M NaOH for 15 min at 100 °C) (*73*) and the digestate was analysed for Mg, K, Ca, Al, and Fe concentrations using inductively coupled plasma-mass spectrometry (ICP-MS, Agilent 7500a). The bSi contained 0.4 ± 0.1 wt% Fe,

consistent with previously observed relative high concentrations of Fe incorporation into *T. pseudonana* frustules (*74*). Concentrations of Mg, K, Ca, Al were below the detection limits.

1.2. Batch experiments

Batch experiments were conducted under simulated sedimentary conditions with different combinations of $Fe(OH)_3$, $Al(OH)_3$, and bSi solids, each at 0.1 g/L, suspended in anoxic artificial seawater (ASW) (*75*) (pH 7.5, buffered with 15 mM HEPES) with 150 μM $Si(OH)_4$. Anoxic DI water was prepared by UV-sterilization and bubbling with ultra-high-purity nitrogen gas. Anoxic ASW was prepared in a glove box (Coy; 95/5 N_2/H_2) using the anoxic DI water. The experimental pH of 7.5 is similar to the condition of Amazon sediment pore waters (*23*). The addition of 150 μM dissolved $Si(OH)_4$ (as Na_2SiO_3) simulates the observed pore water $Si(OH)_4$ concentration for the upper 100 cm of Amazon Delta sediments (*23*) and Mississippi sediments (*22, 28*). Dissolved Fe(II) was added (as $FeCl_2$) to the reaction suspension at 0, 100 μM (Amazon shelf deposit sediments (*76*)), or 1000 μM (representing its concentration in the upper 20 cm of Congo River fan sediments (*38*) and Amazon Delta porewaters (*21*)). The use of amorphous $Al(OH)_3$ was based on that $Al(OH)_3$ is usually a weathering product of Al-bearing lithogenic phases (*77*). The experiments were conducted at room temperature (25 °C), similar to the temperature (28 °C) reported for the Amazon Delta sediment (*23*).

Experiments were conducted in an anoxic glove box using custom-built PVC reactors (7.6 cm) with two chambers (bSi chamber and mineral chamber) separated by a dialysis membrane (12–14 kD, 47 mm; Spectra/Por®) (Figure S1). Each chamber contained 40 mL reaction suspension. The reactor assemblies were acid washed and UV sterilized prior to use. Two sets of experimental groups were set up, with or without bSi. Experimental conditions and sample labels

500 are summarized in Table 1 for Group I with bSi and Table S1 for Group II and III without bSi. For
501 Group I, the bSi substrate was contained in one chamber and the Al/Fe minerals in the other
502 chamber, such that any transformation involving Al/Fe minerals can be attributed to a dissolution-
503 reprecipitation reaction. This also allowed the sampling and structural characterization of
504 transformation products of bSi without the interference from the Al/Fe minerals. For Group II and
505 III, a set of control experiment was conducted with 150 μM dissolved $Si(OH)_4$ (DSi), instead of
506 bSi, with or without Al/Fe minerals. An additional control experiment was conducted with no bSi
507 and only dissolved phases of 150 μM $Si(OH)_4$ (as Na_2SiO_3), 100 μM Fe(II) (as $FeCl_2$), and 30 μM
508 Al^{3+} (as $AlCl_3$). All experiments were conducted in duplicates. Experimental conditions and
509 sample labels are summarized in Table 1 for Group I (with bSi) and Table S1 for Groups II and III
510 (without bSi).

511 Sample-loaded reactors were constantly agitated on a shaker table (120 rpm), assuming
512 that the concentration of ions at each side of the chamber were homogenized through constant
513 shaking. Mixing times when chambers are rolled slowly (e.g., 2 rotations per minute) is on the
514 order of one day (Figure S6); therefore, the shaking likely facilitated well-mixed conditions. The
515 mineral chamber (loaded with Al/Fe minerals) had a hole at the end, which was sealed with silicone
516 stoppers and epoxy. Aliquots of the suspensions were collected periodically using a 1 mm needle
517 through the silicone stoppers, and the liquids were syringe filtered (0.1 μm, PTFE) and analysed
518 for solution composition. At the end of reactions, final solid phases were harvested from both
519 chambers, repeatedly rinsed with anoxic DI water under vacuum filtration, dried in the glove box,
520 and characterized for morphological and structural features.

521

522 **1.3. Aqueous phase analyses**

At each sampling point, dissolved total Fe (Fe_T) and Fe(II) were quantified using the ferrozine spectrophotometric method with or without hydroxylamine, respectively (*78*). Dissolved $Si(OH)_4$ was quantified with the molybdenum blue spectrophotometric method (*79*) using a UV-vis spectrometry (Cary 60, Agilent). Concentrations of dissolved Al were measured by ICP-MS (Agilent 7500a).

1.4. Solid Phase analyses

For experimental groups containing bSi, reacted solids from both chambers were dried on filter membranes inside the anoxic glove box. Solid phases from the bSi chamber were characterized for bSi morphology using scanning electron microscopy (SEM; Hitachi SU-8230) and energy dispersive X-ray spectroscopy (EDX). For groups showing signs of new phase formation under SEM, the solids from both sides of the chamber were further characterized by synchrotron XRD and high-resolution transmission electron microscopy (HRTEM). For synchrotron XRD analysis, solids were sealed into glass capillaries inside the glove box and the data was collected at Beamline 17-BM-B (λ = 0.39433 Å) at Advanced Photon Source (APS; Argonne National Laboratory, Lemont, IL). Based on XRD analysis, the solids at the bSi chamber of the 1000Fe(II)+bSi+Al group showed signs of authigenic clay phase formation, and were further analysed and compared with a control group 1000Fe(II)+bSi using HRTEM (JEOL JEM-2100 LaB6 TEM, 200 KeV accelerating voltage), selected area electron diffraction (SAED; Gatan Orius SC200D camera), and EDX (Bruker AXS Microanalysis Quantax 200 with 4030 SDD detector).

2. Converting Si reaction rate from lab experiments to marine sedimentary conditions

2.1. Reaction rate obtained from lab experiments

In order to compare lab results with field data, we define the reaction rate in lab experiment as the change in reacted concentration over time, which is similar to field studies that estimate and ascribe observed Si fluxes at seasonal time scale (*21*). As the measured apparent dissolved $Si(OH)_4$ is affected by both dissolution and reprecipitation, which cannot fully represent the reacted $Si(OH)_4$, the $Si(OH)_4$ reaction rate we calculated here was based on reacted Fe^{2+} concentration within our experiment time frame and Fe/Si ratio. Our experiment monitored the reaction for over a month and the Fe-annite authigenic clay product were observed to have formed over one month, we then define the reaction time as one month and first calculated monthly reaction rate. The monthly reaction rate of dissolved $Si(OH)_4$ during the transformation of bSi to authigenic clay was estimated based on the amount of reacted Fe^{2+} within 1 month (~ 500 μmol/L for treatment 1000Fe(II)+bSi+Al) and the Fe/Si ratio in the reaction products (detailed in Eqs. 2 and 3 below). The obtained monthly rate was then converted to yearly rate by multiplying 12 (Eq. 4). For a complete transformation to annite, the literature reported stoichiometric Fe/Si ratio of pure annite phase is 1. For authigenic products observed from previous field extraction and SEM studies, this ratio typically varies with an average value of ~0.13 (*21*). This value is a lump sum of different Fe-bearing authigenic products and like intermediate or immature authigenic products. The Fe/Si ratio in the authigenic products in this study observed by SEM varied at 0.5–1. Thus, we used a value of 0.75 for Fe/Si ratio.

The calculated $Si(OH)_4$ rates with a unit of μmol/L/month directly derived from the experimental data are displayed in Table S2.

2.2. Reaction rate conversion to sediment condition

The translation of $Si(OH)_4$ reaction rate from laboratory condition to field sedimentary

569 condition is based on the lab experimental conditions, a field observed average porosity of ~0.7,
570 and sediment density of 2.6 g/cm^3 (*21*), with the assumptions that our experimental condition is
571 comparable to deltaic environments with sufficient Fe and Al mineral supplies (*21, 28*). To be
572 comparable to estimated field sediment Si flux rate, which is measured by reacted $Si(OH)_4$ over
573 dry sediment solid mass with units of μmol/g/yr or μmol/cm^3/yr (interchangeable by average
574 sediment density) (*21, 60*), we then ascribe the reacted solutes to comparable amounts of sediment
575 solid volume in field sediment condition. With weight percentage of typical bSi concentration in
576 marine sediments at 1 to 2 wt%) (*21, 80*), this method assumes a bSi concentration of 1 wt%. Then
577 the 0.1g bSi used in this study is ascribed to 10 g sediments. Applying average sediment porosity
578 of 0.7 and density of 2.6 g/cm^3 typical for delta environments (*21*), the conversion of 10 g sediment
579 to sediment volume is through dividing density (2.6 g/cm^3) and porosity (0.7) (*21*). Thus, 10 g
580 sediment is with a volume of 12.8 cm^3. Therefore, the reacted $Si(OH)_4$ is ascribed to 12.8 cm^3 of
581 sediment (Eq. 4), which is observed in dry sediment solids extraction. The converted $Si(OH)_4$ rate
582 was summarized in Table S2.
583
584 Monthly Fe^{2+} reaction rate at lab condition (μmol/L/month)
585 $$\frac{\mathrm{d}(Fe^{2+})}{dt} = \frac{\text{Reacted } Fe^{2+}}{time} = \frac{500\ \mu\text{mol/L}}{1\ month} \qquad \text{(Eq. 2)}$$
586
587 Monthly $Si(OH)_4$ reaction rate at lab condition (μmol/L/month) can be calculated by:
588 $$\frac{1}{f} * \frac{\mathrm{d}(Fe^{2+})}{dt} = \frac{1}{s} * \frac{\mathrm{d}(\mathrm{Si(OH)4})}{dt}$$, Where f/s = Fe/Si ratio in authigenic phase (Eq. 3)
589
590 Yearly $Si(OH)_4$ reaction rate at lab condition (μmol/L/yr)
591 = $Si(OH)_4$ reaction rate at lab condition per month * 12 months/1 yr (Eq. 4)

Yearly $Si(OH)_4$ reaction rate at field sedimentary condition (μmol/cm^3/yr)

$$\frac{\text{Yearly Si(OH)4 reaction rate at lab condition in μmol /L/yr} * 1\ \text{L}}{12.8\ \text{cm3}}$$

$$= \frac{\text{Si(OH)4 reaction rate at lab condition in μmol/yr}}{12.8\ \text{cm3}} \quad \text{(Eq.5)}$$

2.3. Estimation of reverse weathering rate coefficient and Si sink

Assuming the reaction rate (Rw) of reverse weathering is zero order with respect to dissolved $Si(OH)_4$ (*21*), i.e., $Rw = k * [Si(OH)_4]^0$, then the reaction rate coefficient (k) is equivalent to the reaction rate of dissolved $Si(OH)_4$ (Eq. 5).

$$-\frac{d(Si(OH)4)}{dt} = k \quad \text{(Eq. 6)}$$

Thus the rate coefficient can be calculated in μmol/cm^3/s and compared with literature reverse weathering reaction rates (Table S3).

Acknowledgements

This work is funded by the National Science Foundation grants OCE-1559087 (YT) and OCE-1558957 (JWK).

Data Availability

A full compilation of solution phase data in the main text and SI are available through Mendeley data at: https://data.mendeley.com/preview/9w48g2sfp7?a=b005c369-43d8-4393-8b27-ad97c14eb340

Author contributions

E.M.S. and Y.T. conceived of the experiments with input from R.A.P. and J.W.K. E.M.S. led the primary experiments and sample analysis with assistance from S.Z., P.L., H.Z., L.Z. and H.D; S.Z. and E.M.S analyzed the data and interpreted the results. S.Z. and E.M.S. wrote the manuscript,

with guidance from Y.T. and J.W.K., and input from all authors.

Competing interests

The authors declare no competing interests.

References

1. F. T. Mackenzie, R. M. Garrels, Chemical mass balance between rivers and oceans. *American Journal of Science* **264**, 507-525 (1966).
2. R. M. Garrels, SILICA - ROLE IN BUFFERING OF NATURAL WATERS. *Science* **148**, 69-& (1965).
3. F. T. Mackenzie, R. M. Garrels, SILICA-BICARBONATE BALANCE IN OCEAN AND EARLY DIAGENESIS. *Journal of Sedimentary Petrology* **36**, 1075-+ (1966).
4. F. T. Mackenzie, R. M. Garrels, O. P. Bricker, F. Bickley, SILICA IN SEA WATER - CONTROL BY SILICA MINERALS. *Science* **155**, 1404-+ (1967).
5. P. Michalopoulos, R. C. Aller, R. J. Reeder, Conversion of diatoms to clays during early diagenesis in tropical, continental shelf muds. *Geology* **28**, 1095-1098 (2000).
6. T. T. Isson, N. J. Planavsky, Reverse weathering as a long-term stabilizer of marine pH and planetary climate. *Nature* **560**, 471-475 (2018).
7. T. T. Isson *et al.*, Evolution of the Global Carbon Cycle and Climate Regulation on Earth. *Global Biogeochemical Cycles* **34**, e2018GB006061 (2020).
8. J. Krissansen-Totton, D. C. Catling, A coupled carbon-silicon cycle model over Earth history: Reverse weathering as a possible explanation of a warm mid-Proterozoic climate. *Earth and Planetary Science Letters* **537**, 116181 (2020).
9. S. Loucaides *et al.*, Seawater-mediated interactions between diatomaceous silica and terrigenous sediments: results from long-term incubation experiments. *Chemical Geology* **270**, 68-79 (2010).
10. P. J. Treguer, C. L. De La Rocha, in *Annual Review of Marine Science, Vol 5,* C. A. Carlson, S. J. Giovannoni, Eds. (Annual Reviews, Palo Alto, 2013), vol. 5, pp. 477-501.
11. S. Rahman, R. C. Aller, J. K. Cochran, The Missing Silica Sink: Revisiting the Marine Sedimentary Si Cycle Using Cosmogenic 32Si. *Global Biogeochemical Cycles* **31**, 1559-1578 (2017).
12. P. J. Tréguer *et al.*, Reviews and syntheses: The biogeochemical cycle of silicon in the modern ocean. *Biogeosciences* **18**, 1269-1289 (2021).
13. O. Ragueneau, D. J. Conley, D. J. DeMaster, H. H. Durr, N. Dittert, in *Carbon and Nutrient Fluxes in Continental Margins: A Global Synthesis,* K. K. Liu, L. Atkinson, R. Quinones, L. TalaueMcManus, Eds. (2010), pp. 515-527.
14. S. Foteinis, J. S. Campbell, P. Renforth, Life Cycle Assessment of Coastal Enhanced Weathering for Carbon Dioxide Removal from Air. *Environmental Science & Technology* **57**, 6169-6178 (2023).
15. Y. Kanzaki, N. J. Planavsky, C. T. Reinhard, New estimates of the storage permanence and ocean co-benefits of enhanced rock weathering. *PNAS Nexus* **2**, pgad059 (2023).
16. G. S. Odin, F. Fröhlich, Chapter C3 Glaucony from the Kerguelen Plateau (Southern Indian Ocean). *Developments in Sedimentology* **45**, 277-294 (1988).
17. J. E. Mackin, CONTROL OF DISSOLVED AL DISTRIBUTIONS IN MARINE-SEDIMENTS BY CLAY RECONSTITUTION REACTIONS - EXPERIMENTAL-EVIDENCE LEADING TO A UNIFIED THEORY. *Geochimica Et Cosmochimica Acta* **50**, 207-214 (1986).
18. J. E. Mackin, R. C. Aller, DISSOLVED AL IN SEDIMENTS AND WATERS OF THE EAST CHINA SEA - IMPLICATIONS FOR AUTHIGENIC MINERAL FORMATION. *Geochimica Et Cosmochimica Acta* **48**, 281-297 (1984).

19. J. E. Mackin, R. C. Aller, THE EFFECTS OF CLAY MINERAL REACTIONS ON DISSOLVED AL DISTRIBUTIONS IN SEDIMENTS AND WATERS OF THE AMAZON CONTINENTAL-SHELF. *Continental Shelf Research* **6**, 245-262 (1986).
20. J. R. Hein, H.-W. Yeh, E. Alexander, Origin of Iron-Rich Montmorillonite from the Manganese Nodule Belt of the North Equatorial Pacific. *Clays and Clay Minerals* **27**, 185-194 (1979).
21. P. Michalopoulos, R. C. Aller, Early diagenesis of biogenic silica in the Amazon delta: Alteration, authigenic clay formation, and storage. *Geochimica Et Cosmochimica Acta* **68**, 1061-1085 (2004).
22. R. A. Pickering *et al.*, Using Stable Isotopes to Disentangle Marine Sedimentary Signals in Reactive Silicon Pools. *Geophysical Research Letters*, (2020).
23. P. Michalopoulos, R. C. Aller, Rapid clay mineral formation in Amazon delta sediments: reverse weathering and oceanic elemental cycles. *Science*, 614-614 (1995).
24. R. S. Arvidson, F. T. Mackenzie, M. Guidry, MAGic: A Phanerozoic model for the geochemical cycling of major rock-forming components. *American Journal of Science* **306**, 135-190 (2006).
25. K. L. Russell, GEOCHEMISTRY AND HALMYROLYSIS OF CLAY MINERALS, RIO-AMECA, MEXICO. *Geochimica Et Cosmochimica Acta* **34**, 893-& (1970).
26. J. I. Drever, EARLY DIAGENESIS OF CLAY-MINERALS RIO-AMECA BASIN, MEXICO. *Journal of Sedimentary Petrology* **41**, 982-& (1971).
27. F. T. Mackenzie, L. R. Kump, Reverse Weathering, Clay Mineral Formation, and Oceanic Element Cycles. *Science* **270**, 586 (1995).
28. M. Presti, P. Michalopoulos, Estimating the contribution of the authigenic mineral component to the long-term reactive silica accumulation on the western shelf of the Mississippi River Delta. *Continental Shelf Research* **28**, 823-838 (2008).
29. S. Loucaides *et al.*, Seawater-mediated interactions between diatomaceous silica and terrigenous sediments: Results from long-term incubation experiments. *Chemical Geology* **270**, 68-79 (2010).
30. R. A. Pickering *et al.*, Using Stable Isotopes to Disentangle Marine Sedimentary Signals in Reactive Silicon Pools. *Geophysical Research Letters* **47**, e2020GL087877 (2020).
31. R. C. Aller, in *Treatise on Geochemistry, Second Edition,* H. H.D., T. K.K., Eds. (Elsevier, Oxford, 2014), vol. 8, pp. 293-334.
32. D. M. Moore, *X-ray diffraction and the identification and analysis of clay minerals / Duane M. Moore and Robert C. Reynolds, Jr*. R. C. Reynolds, Ed., (Oxford University Press, Oxford [England] ;, 1989).
33. S. M. Chemtob, R. D. Nickerson, R. V. Morris, D. G. Agresti, J. G. Catalano, Synthesis and structural characterization of ferrous trioctahedral smectites: Implications for clay mineral genesis and detectability on Mars. *Journal of Geophysical Research: Planets* **120**, 1119-1140 (2015).
34. G. J. Redhammer, A. Beran, J. Schneider, G. Amthauer, W. Lottermoser, Spectroscopic and structural properties of synthetic micas on the annite-siderophyllite binary: Synthesis, crystal structure refinement, Mössbauer, and infrared spectroscopy. *American Mineralogist* **85**, 449-465 (2000).
35. J. P. Gustafsson. (Stockholm, 2016).
36. D. Rickert, M. Schlüter, K. Wallmann, Dissolution kinetics of biogenic silica from the water column to the sediments. *Geochimica et Cosmochimica Acta* **66**, 439-455 (2002).

37. P. VanCappellen, L. Q. Qiu, Biogenic silica dissolution in sediments of the Southern Ocean .2. Kinetics. *Deep-Sea Research Part Ii-Topical Studies in Oceanography* **44**, 1129-1149 (1997).
38. J. S. Beckler, N. Kiriazis, C. Rabouille, F. J. Stewart, M. Taillefert, Importance of microbial iron reduction in deep sediments of river-dominated continental-margins. *Marine Chemistry* **178**, 22-34 (2016).
39. P. Van Cappellen, S. Dixit, J. van Beusekom, Biogenic silica dissolution in the oceans: Reconciling experimental and field-based dissolution rates. *Global Biogeochemical Cycles* **16**, (2002).
40. O. Ragueneau, S. Schultes, K. Bidle, P. Claquin, B. La Moriceau, Si and C interactions in the world ocean: Importance of ecological processes and implications for the role of diatoms in the biological pump. *Global Biogeochemical Cycles* **20**, (2006).
41. M. Maldonado *et al.*, Sponge skeletons as an important sink of silicon in the global oceans. *Nature Geoscience* **12**, 815-822 (2019).
42. D. E. Canfield, K. Erik, T. Bo, in *Advances in Marine Biology,* D. E. Canfield, E. Kristensen, B. Thamdrup, Eds. (Academic Press, 2005), vol. 48, pp. 441-463.
43. N. Llopis Monferrer *et al.*, Estimating Biogenic Silica Production of Rhizaria in the Global Ocean. *Global Biogeochemical Cycles* **34**, e2019GB006286 (2020).
44. P. VanCappellen, L. Q. Qiu, Biogenic silica dissolution in sediments of the Southern Ocean .1. Solubility. *Deep-Sea Res. Part II-Top. Stud. Oceanogr.* **44**, 1109-1128 (1997).
45. S. Dixit, P. Van Cappellen, Surface chemistry and reactivity of biogenic silica. *Geochimica Et Cosmochimica Acta* **66**, 2559-2568 (2002).
46. J. C. Lewin, The dissolution of silica from diatom walls. *Geochimica Et Cosmochimica Acta* **21**, 182-198 (1961).
47. R. K. Iler, *The Chemistry of Silica*. (Wiley- Interscience, New York, 1979).
48. A. J. Vanbennekom, J. H. F. Jansen, S. J. Vandergaast, J. M. Vaniperen, J. Pieters, ALUMINUM-RICH OPAL - AN INTERMEDIATE IN THE PRESERVATION OF BIOGENIC SILICA IN THE ZAIRE (CONGO) DEEP-SEA FAN. *Deep-Sea Research Part a-Oceanographic Research Papers* **36**, 173-190 (1989).
49. M. Kosmulski, *Surface charging and points of zero charge*. Surfactant science series (CRC Press, Boca Raton, 2009), pp. xxvii, 1064 p.
50. X. Zhang, J. Gaillardet, L. Barrier, J. Bouchez, Li and Si isotopes reveal authigenic clay formation in a palaeo-delta. *Earth and Planetary Science Letters* **578**, 117339 (2022).
51. D. Badaut, F. Risacher, Authigenic smectite on diatom frustules in Bolivian saline lakes. *Geochimica et Cosmochimica Acta* **47**, 363-375 (1983).
52. M. Pozo, J. P. Calvo, An Overview of Authigenic Magnesian Clays. *Minerals* **8**, (2018).
53. J. Kim *et al.*, Naturally occurring, microbially induced smectite-to-illite reaction. *Geology* **47**, 535-539 (2019).
54. M. Robert, The Experimental Transformation of Mica Toward Smectite; Relative Importance of Total Charge and Tetrahedral Substitution. *Clays and Clay Minerals* **21**, 167-174 (1973).
55. K. D. Bidle, F. Azam, Bacterial control of silicon regeneration from diatom detritus: Significance of bacterial ectohydrolases and species identity. *Limnology and Oceanography* **46**, 1606-1623 (2001).
56. E. M. Saad *et al.*, Effect of Cleaning Methods on the Dissolution of Diatom Frustules. *Marine Chemistry* **224**, (2020).

57. D. J. DeMaster, in *Treatise on Geochemistry,* H. D. Holland, K. K. Turekian, Eds. (Pergamon, Oxford, 2003), pp. 87-98.
58. F. Fraysse, O. S. Pokrovsky, J. Schott, J.-D. Meunier, Surface chemistry and reactivity of plant phytoliths in aqueous solutions. *Chemical Geology* **258**, 197-206 (2009).
59. G. G. Laruelle *et al.*, Anthropogenic perturbations of the silicon cycle at the global scale: Key role of the land-ocean transition. *Global Biogeochemical Cycles* **23**, (2009).
60. S. Rahman, R. C. Aller, J. K. Cochran, Cosmogenic 32Si as a tracer of biogenic silica burial and diagenesis: Major deltaic sinks in the silica cycle. *Geophysical Research Letters* **43**, 7124-7132 (2016).
61. P. A. Maurice, *Environmental surfaces and interfaces from the nanoscale to the global scale*. (Wiley, 2009).
62. W. Stumm, J. J. Morgan, *Aquatic chemistry : chemical equilibria and rates in natural waters*. (New York : Wiley, ed. 3rd ed., 1996).
63. J. Aubineau *et al.*, Microbially induced potassium enrichment in Paleoproterozoic shales and implications for reverse weathering on early Earth. *Nature Communications* **10**, 2670 (2019).
64. J. Cuadros, Clay minerals interaction with microorganisms: a review. *Clay Minerals* **52**, 235-261 (2017).
65. M. Ueshima, K. Tazaki, Possible Role of Microbial Polysaccharides in Nontronite Formation. *Clays and Clay Minerals* **49**, 292-299 (2001).
66. S. Geilert *et al.*, Coastal El Niño triggers rapid marine silicate alteration on the seafloor. *Nature Communications* **14**, 1676 (2023).
67. H. Jurikova, Reversing Earth's carbon engine. *Nature Geoscience* **15**, 756-757 (2022).
68. C. Cao *et al.*, Persistent late Permian to Early Triassic warmth linked to enhanced reverse weathering. *Nature Geoscience* **15**, 832-838 (2022).
69. T. T. Isson *et al.*, Marine siliceous ecosystem decline led to sustained anomalous Early Triassic warmth. *Nature Communications* **13**, 3509 (2022).
70. Y. Z. Tang *et al.*, Structural Properties of the Cr(III)-Fe(III) (Oxy)hydroxide Compositional Series: Insights for a Nanomaterial "Solid Solution". *Chem. Mat.* **22**, 3589-3598 (2010).
71. T. Isobe, T. Watanabe, J. B. D. de la Caillerie, A. P. Legrand, D. Massiot, Solid-state H-1 and Al-27 NMR studies of amorphous aluminum hydroxides. *Journal of Colloid and Interface Science* **261**, 320-324 (2003).
72. J. I. Hedges, J. H. Stern, Carbon and nitrogen determinations of carbonate-containing solids. *Limnology and Oceanography* **29**, 657-663 (1984).
73. G. L. Krausse, C. L. Schelske, C. O. Davis, Comparison of three wet-alkaline methods of digestion of biogenic silica in water. *Freshwater Biology* **13**, 73-81 (1983).
74. M. J. Ellwood, K. A. Hunter, The incorporation of zinc and iron into the frustule of the marine diatom Thalassiosira pseudonana. *Limnology and oceanography* **45**, 1517-1524 (2000).
75. D. R. Kester, I. W. Duedall, D. N. Connors, Pytkowic.Rm, PREPARATION OF ARTIFICIAL SEAWATER. *Limnology and Oceanography* **12**, 176-& (1967).
76. R. C. Aller, N. E. Blair, Q. Xia, P. D. Rude, Remineralization rates, recycling, and storage of carbon in Amazon shelf sediments. *Continental Shelf Research* **16**, 753-786 (1996).
77. M. Kawano, K. Tomita, Amorphous Aluminum Hydroxide Formed at the Earliest Weathering Stages of K-Feldspar. *Clays and Clay Minerals* **44**, 672-676 (1996).

78. L. L. Stookey, Ferrozine---a new spectrophotometric reagent for iron. *Analytical Chemistry* **42**, 779-781 (1970).
79. J. D. Strickland, T. R. Parsons, A practical handbook of seawater analysis. (1972).
80. C. Ehlert *et al.*, Stable silicon isotope signatures of marine pore waters - Biogenic opal dissolution versus authigenic clay mineral formation. *Geochimica Et Cosmochimica Acta* **191**, 102-117 (2016).

Table 1. Summary of treatment conditions and sample labels with bSi. All treatments contain 150 μM background dissolved silica, $Si(OH)_4$. "+" stands for the addition of the reactant.

Treatment group	Dissolved $Si(OH)_4$ (μM)	Dissolved Fe(II) (μM)	bSi	$Fe(OH)_3$	$Al(OH)_3$	Sample label
I (with bSi)	150	0	+			0Fe(II)+bSi
	150	0	+	+		0Fe(II)+bSi+Fe
	150	0	+		+	0Fe(II)+bSi+Al
	150	0	+	+	+	0Fe(II)+bSi+FeAl
	150	100	+			100Fe(II)+bSi
	150	100	+	+		100Fe(II)+bSi+Fe
	150	100	+		+	100Fe(II)+bSi+Al
	150	100	+	+	+	100Fe(II)+bSi+FeAl
	150	1000	+			1000Fe(II)+bSi
	150	1000	+	+		1000Fe(II)+bSi+Fe
	150	1000	+		+	1000Fe(II)+bSi+Al
	150	1000	+	+	+	1000Fe(II)+bSi+FeAl

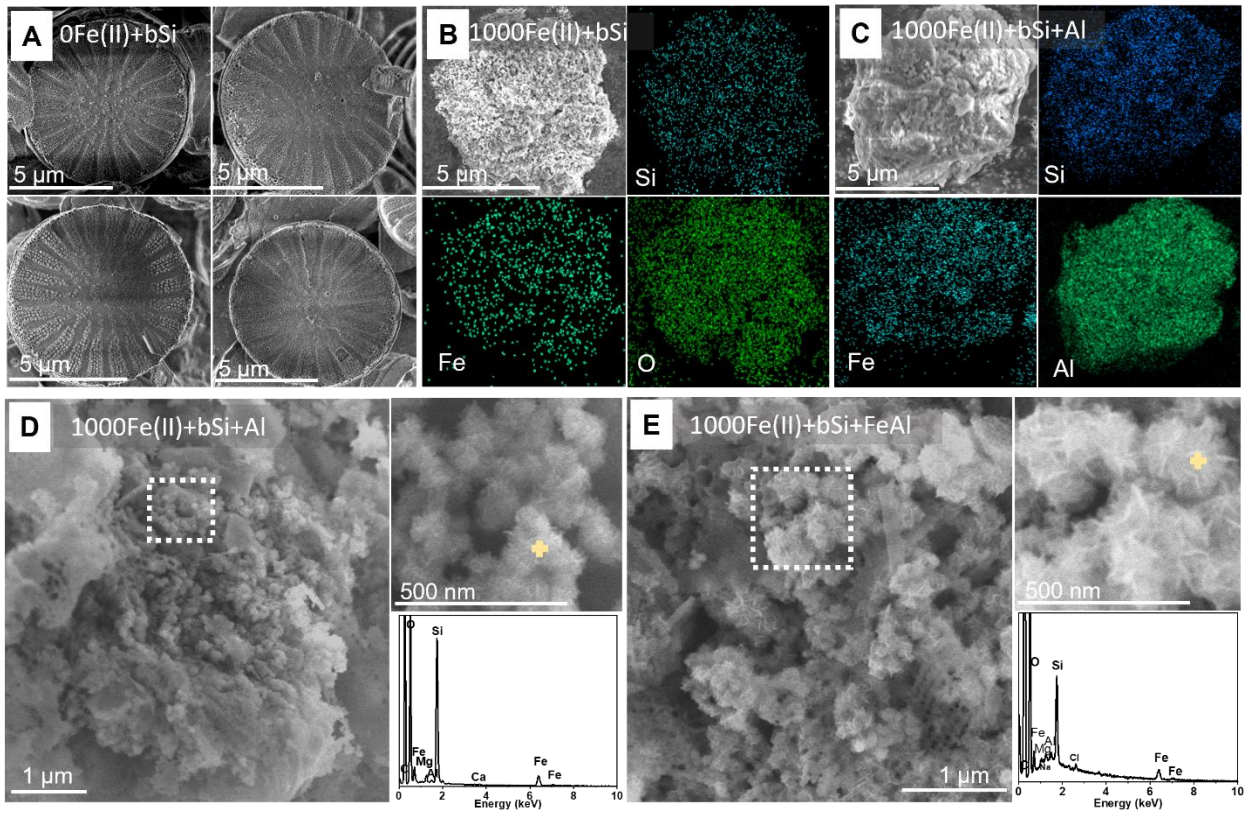

Figure 1. Representative SEM images and EDX elemental maps of reacted $bSiO_2$ after 40 days in 0Fe(II)+bSi (**A**), 1000Fe(II)+bSi (**B**), and 1000Fe(II)+bSi+Al (**C**), as well as the morphology and EDX spectra of new phases formed in 1000Fe(II)+bSi+Al (**D**) and 1000Fe(II)+bSi+FeAl (**E**) treatments. No changes in morphology were observed in 0 μM Fe(II) treatment (**A**), whereas bSi were extensively altered and elemental association of Fe, Si, and O were observed in **B** and **C**. Flake-shaped rosette clusters of new phases were observed in **D** and **E**, with both phase rich in Fe, Si, Al, and Mg. Dashed areas in **D** and **E** show zoomed view with EDX spectra taken at the cross point.

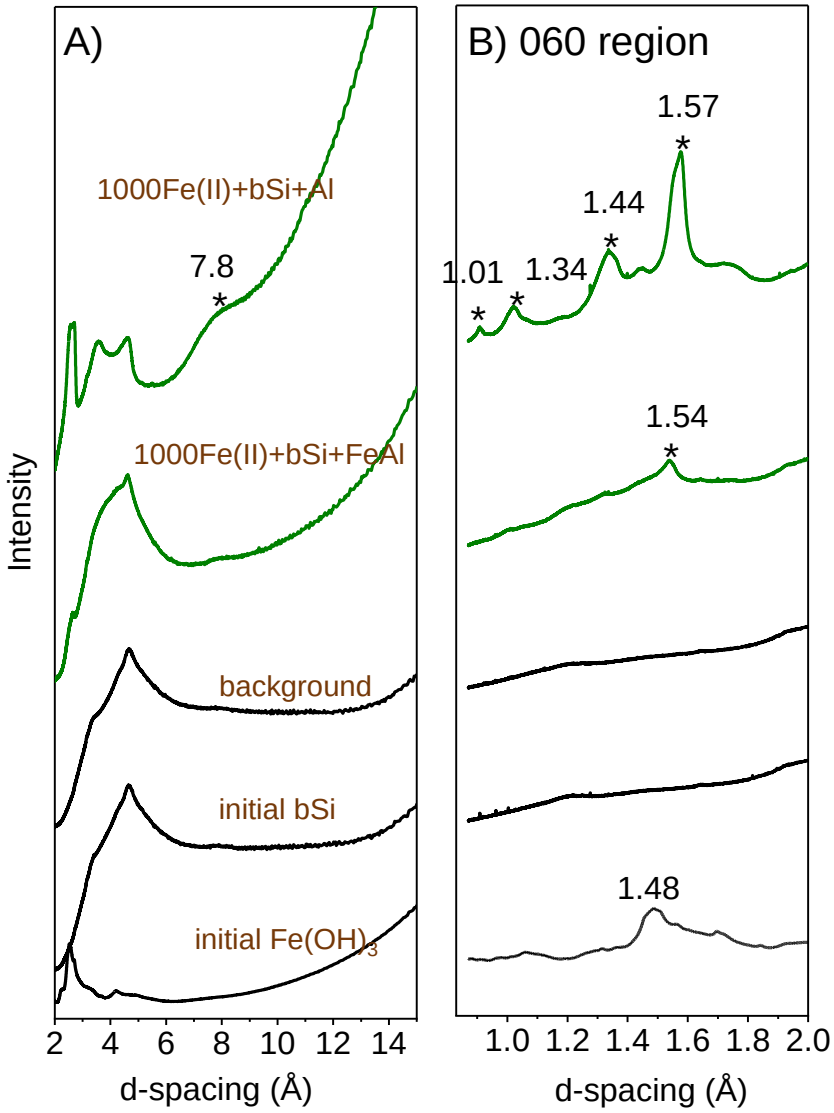

Figure 2. (A) Synchrotron XRD patterns (λ = 0.39433 Å) of reacted solids from 1000Fe(II)+bSi+Al and 1000Fe(II)+bSi+FeAl treatments after 40 days, compared to initial $Fe(OH)_3$, bSi, and background from the glass capillary. Reacted solids were taken from bSi chamber of the two-chamber reactor. Asterisks indicate peaks from the newly formed phase. **(B)** shows a zoomed-view of the d_{060} region from figure **(A)**.

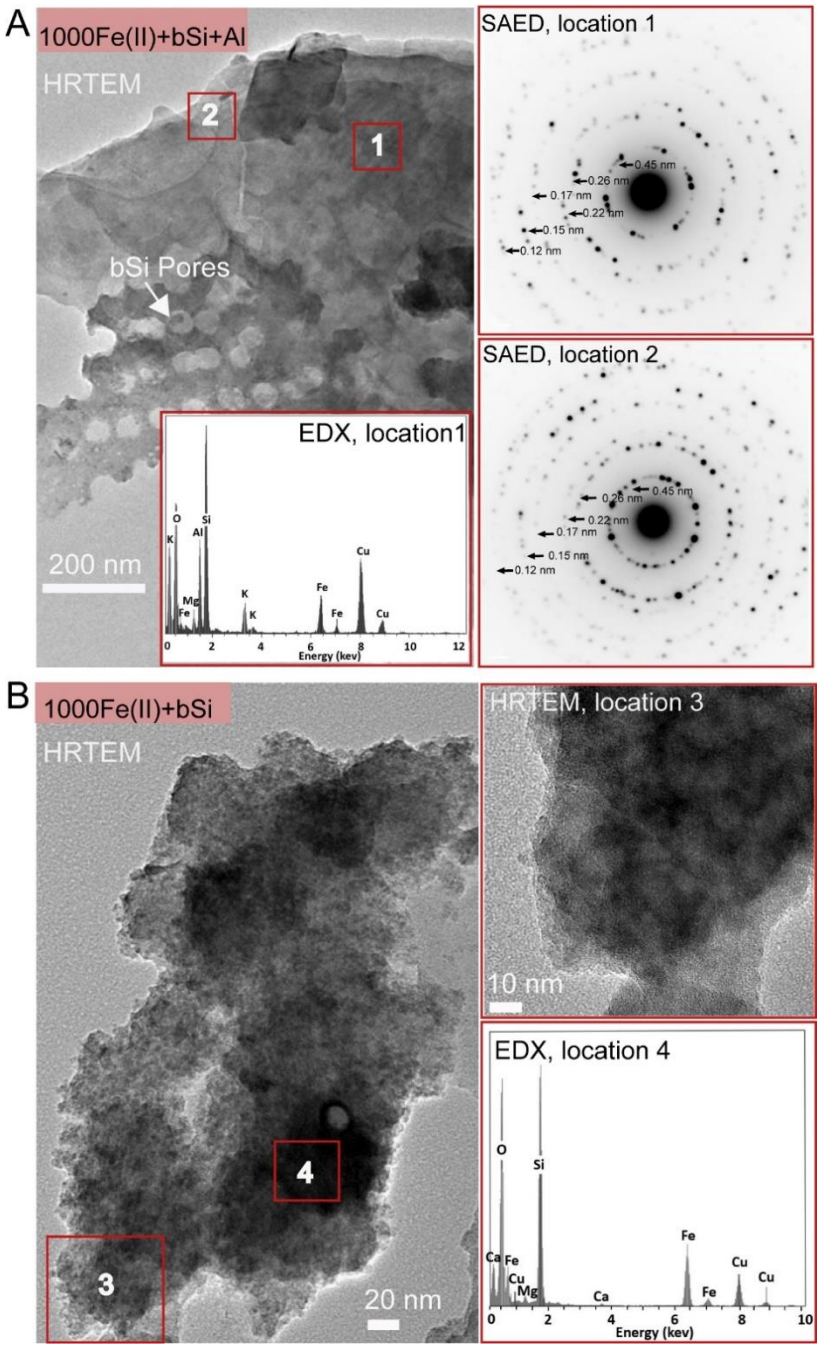

Figure 3. Representative HRTEM images and corresponding SAED and EDX patterns of experiments 1000Fe(II)+bSi+Al (**A**) and 1000Fe(II)+bSi (**B**) for 40 days. Solids were harvested from the bSi side of the two-chamber reactor. (**A**) $bSiO_2$ was extensively altered to form new mineral phases. White arrow indicates the porous morphology of residual diatom bSi. SAED

patterns of locations 1 and 2 show six d-spacings at 0.45, 0.26, 0.22, 0.17, 0.15, and 0.12 nm, characteristic of annite (Fe-rich mica). EDX spectrum of location 1 shows a composition consistent with Fe-muscovite dominated by Si, K, Fe, Al, and Mg. (**B)** $bSiO_2$ was altered to amorphous phase. A zoomed view of location 3 shows no fringe lattice. EDX spectrum of location 4 shows that the amorphous phase is mainly composed of Si, Fe, Ca, and Mg. Copper signal is from the TEM grid.

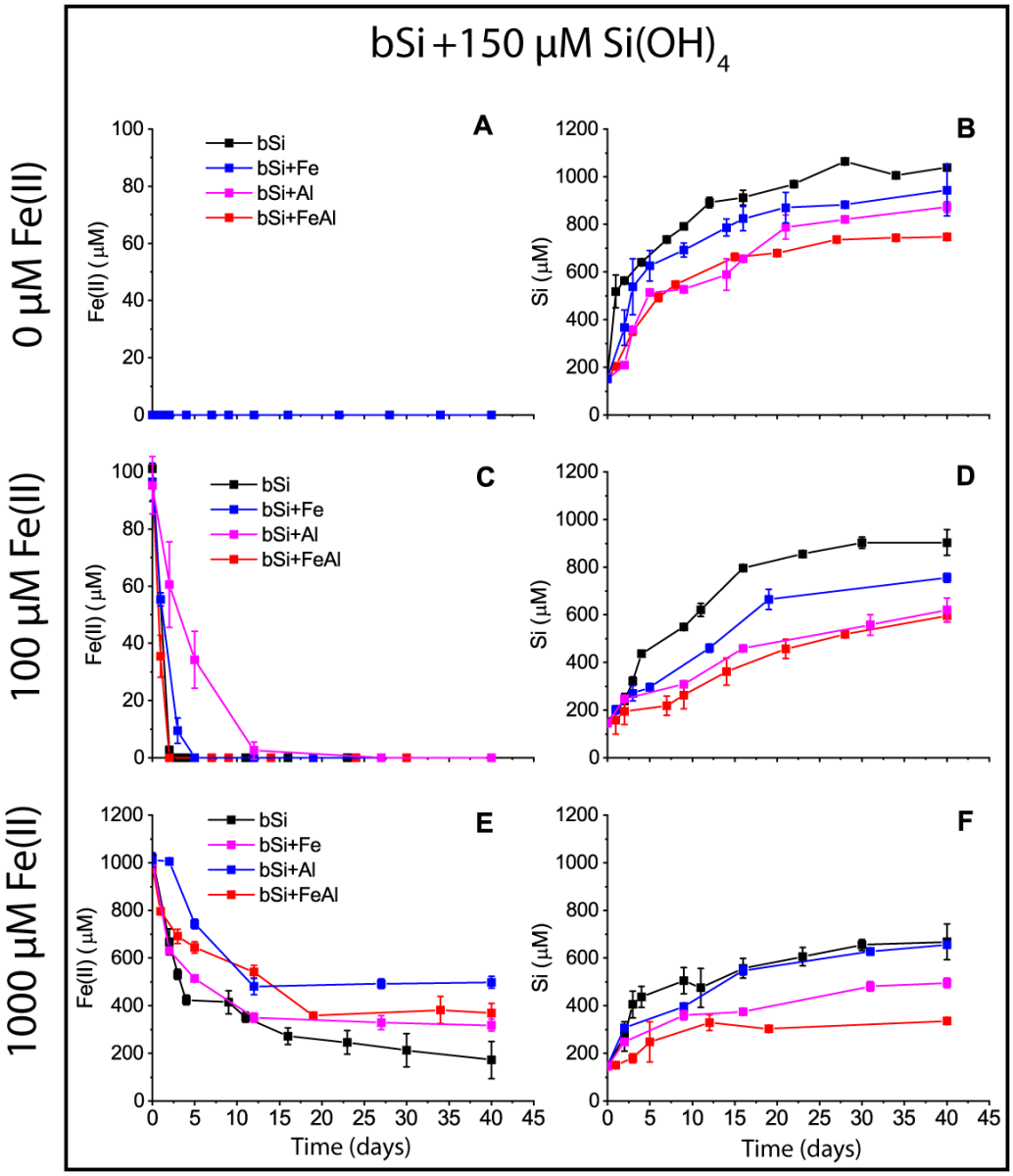

Figure 4. Time evolution of dissolved Fe(II) and apparent dissolved Si in the presence of (**A–F**)

bSi and 150 μM background dissolved $Si(OH)_4$. Top, middle, and bottom panels are treatments with 0 μM , 100 Fe(II), or 1000 μM Fe(II). The prefixes of 0Fe(II), 100Fe(II), and 1000Fe(II) in sample labels are omitted for the top, middle and bottom panels for succinctness. Error bars represent standard deviation of duplicate treatment.

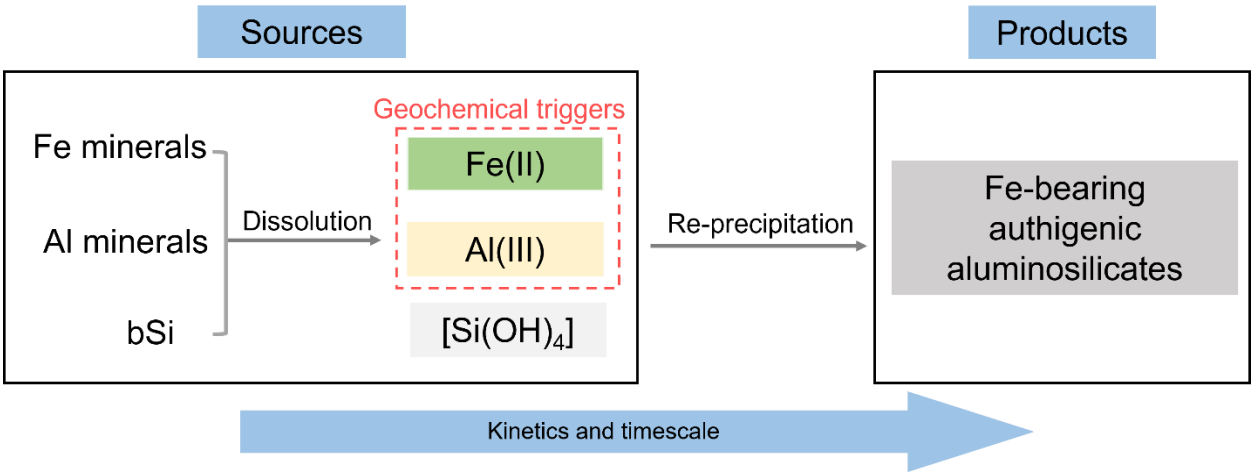

847

848 **Figure 5.** Conceptual illustration of the reverse weathering process in the modern ocean.
849 Illustration of the mechanisms involved in the formation of authigenic clay revealed by this study,
850 indicating the sources (dissolved Fe(II), Al(III), and $Si(OH)_4$ from dissolution of solid phases) and
851 products (formed via re-precipitation).

852

853

854

855

856

857

858

859

860

861

862

863

864

865

Supplementary Information

Rapid transformation of biogenic silica to authigenic clay in reverse weathering

Simin Zhao[1#], Emily M. Saad[1#], Rebecca A. Pickering[2], Pan Liu[1], Hongyan Zuo[3], Linduo Zhao[4], Ellery Ingall[1], Martial Taillefert[1], Christopher T. Reinhard[1], Hailiang Dong[3], Jeffrey W. Krause[2,5]*, Yuanzhi Tang[1]*

[1]School of Earth and Atmospheric Sciences, Georgia Institute of Technology, Atlanta, GA 30332-0340, USA

[2]Stokes School Marine and Environmental Sciences, University of South Alabama, Mobile, AL 36688, USA

[3]Department of Geology & Environmental Earth Science, Miami University, Oxford, OH 45056, USA

[4]Illinois Sustainable Technology Center, University of Illinois at Urbana-Champaign, Champaign, IL 61820, USA

[5]Dauphin Island Sea Lab, Dauphin Island, AL, 36528, USA

[#]Authors contributed equally.

*Corresponding authors: Yuanzhi Tang (yuanzhi.tang@eas.gatech.edu), Jeffrey W. Krause (jkrause@disl.edu)

This PDF file includes:

Supplementary text

Figs. S1 to S7

Tables S1 to S4

References for SI reference citations

Supplementary Text

Section S1. Estimation of CO_2 release by reverse weathering in modern ocean

By knowing the alkalinity (Alk) to silica (Si) ratio (Alk:Si) associated with authigenic clay formation, the reverse weathering-induced flux of CO2 release can be estimated *(1-3)*. The Alk:Si ratio is dependent on the type and composition of the clay product (e.g., kaolinite, smectite, and chlorite type), an range ratio of 1.33–4 is applied in the estimation *(1-3)* depending on mineral type (e.g., 1.33 for sepiolite, 2.33 for saponite and 4 for berthierine). Our observed Fe-annite product, a type of Fe-smectite, is most close to saponite (another Fe-bearing smectite group mineral) applied in these estimations with a Alk:Si ratio of ~2.33 *(1, 2)*.

The previous compilation of global CO_2 source contribution from reverse weathering by Isson et al., 2020 (*1*) was based on the Si sink of 4.5–4.9 T mole/yr and the corresponding translation to CO_2 release of 10 T mole/yr (Table S4). While the most up to date CO_2 release by reverse weathering yield a 10 T mole/yr CO_2, (Table S4).

Figures and Tables

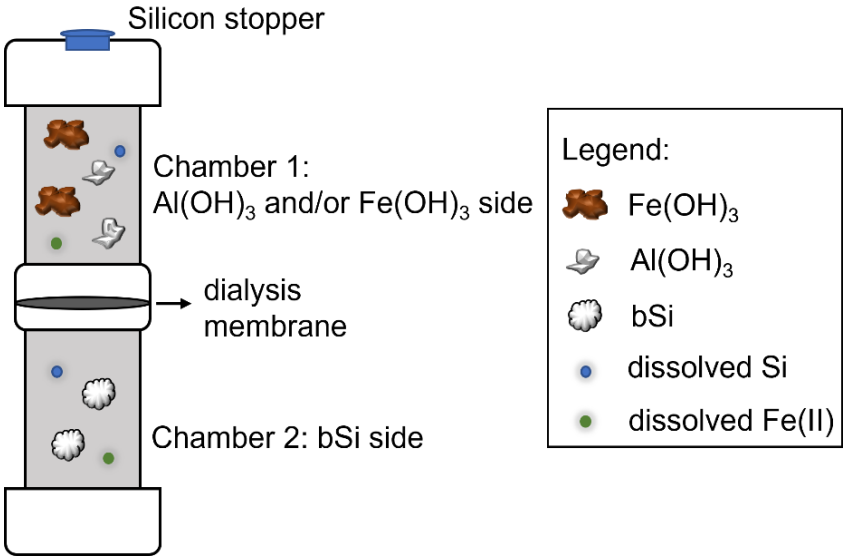

Figure S1. Schematic illustration of the experimental reactor (not to scale) with two chambers separated by a dialysis membrane. bSi is added to one chamber (bSi chamber), and $Al(OH)_3$ and/or $Fe(OH)_3$ minerals are added to the other chamber (mineral chamber).

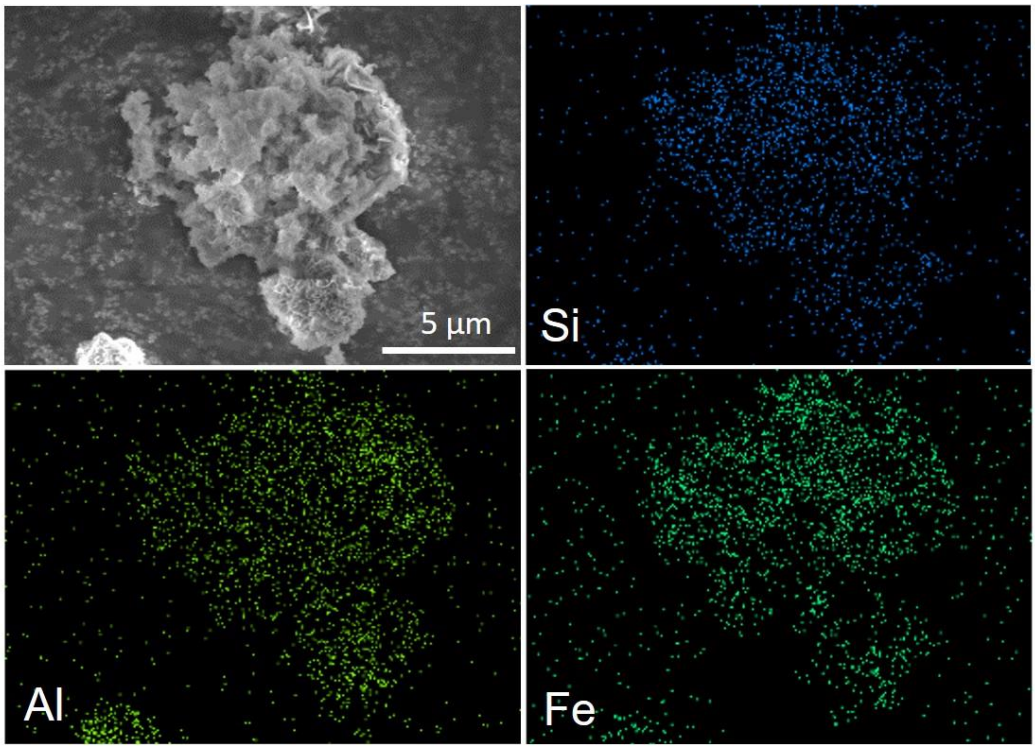

Figure S2. Representative SEM image and EDX elemental maps of layered precipitates for 1000Fe(II)+bSi+Al incubated for 40 days. The new precipitate is enriched in Fe, Al, and Si.

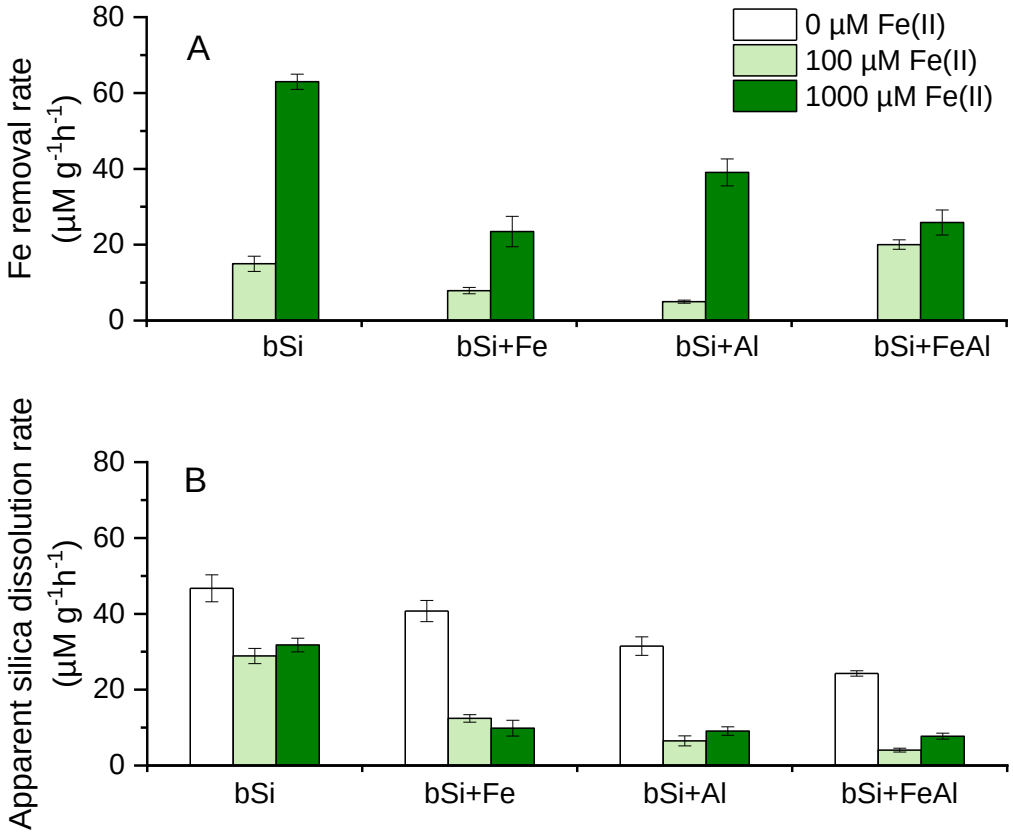

Figure S3. The initial rates for (A) the removal of dissolved Fe(II) and (B) the apparent silica dissolution. Rates were determined by fitting a linear regression line through the concentration evolution profile for the first ~7 days. Error bars represent standard deviation of rate from duplicate treatments.

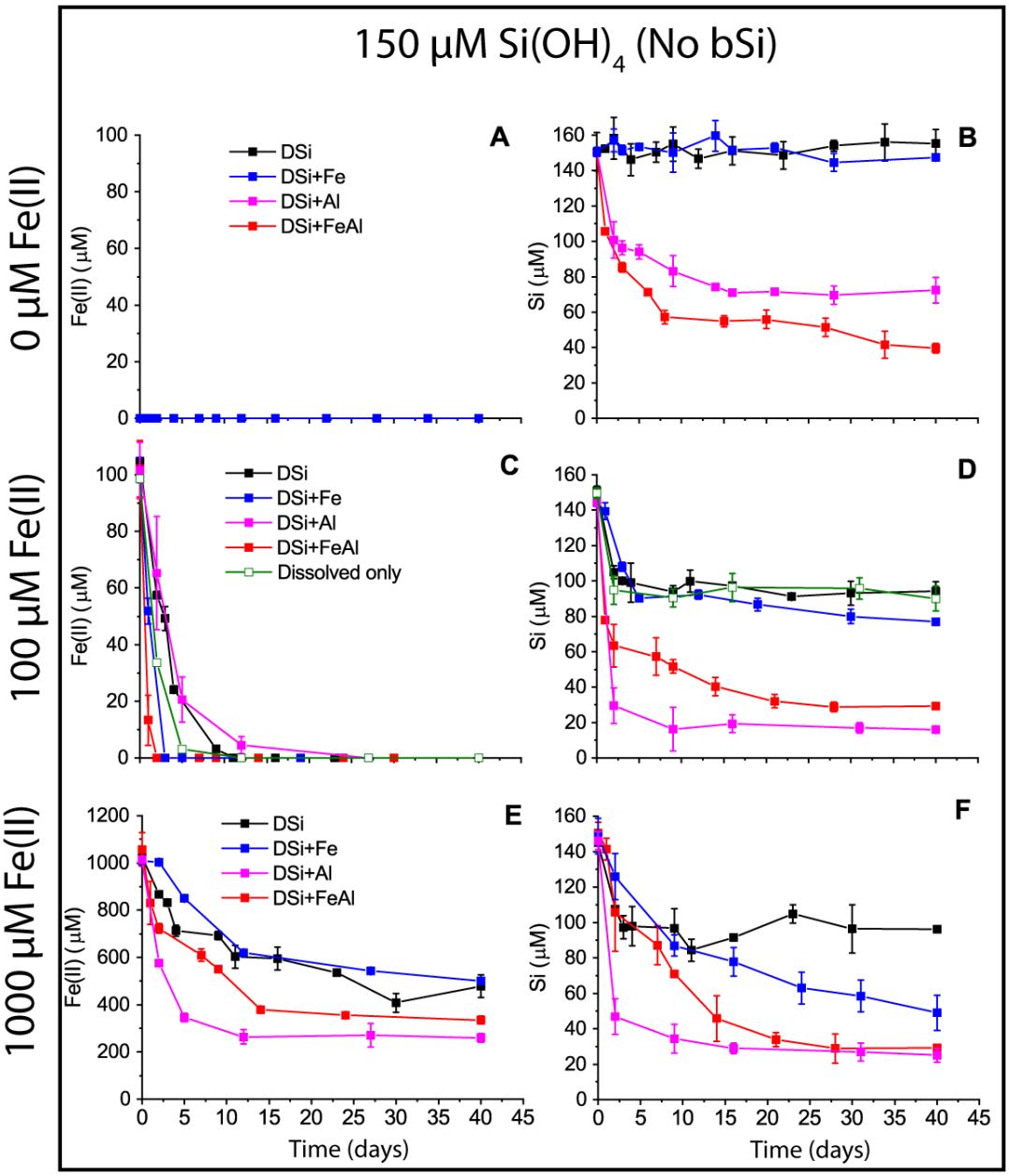

934

935 **Figure S4**. Time evolution of dissolved Fe(II) and Si in the presence of 150 µM dissolved $Si(OH)_4$
936 only. Top, middle, and bottom panels are treatments with 0 µM , 100 Fe(II), or 1000 µM Fe(II).
937 The prefixes of 0Fe(II), 100Fe(II), and 1000Fe(II) in sample labels are omitted for the top, middle
938 and bottom panels for succinctness. Error bars represent standard deviation of duplicate treatments.

939

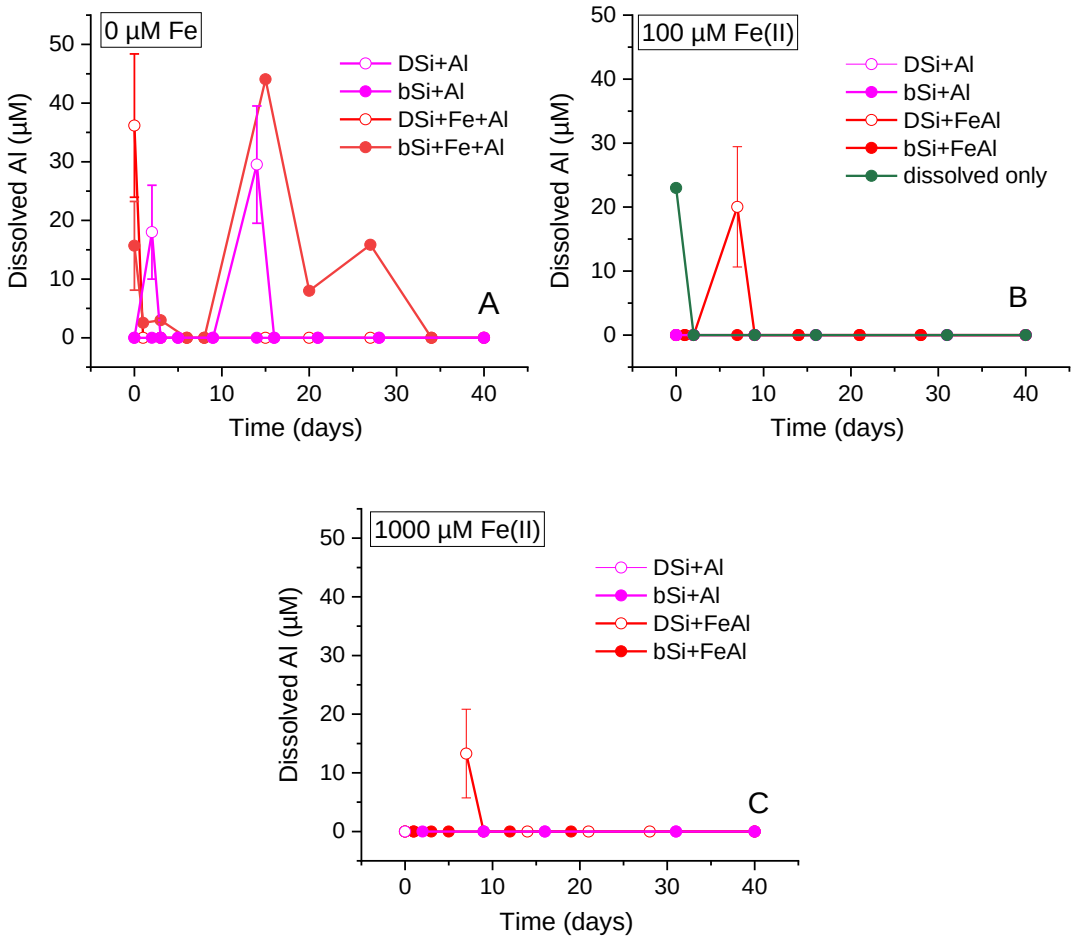

940

941
942

943 **Figure S5.** Dissolved Al from $Al(OH)_3$ in treatments with or without $Fe(OH)_3$ and bSi. (A) 0 µM
944 Fe(II) treatments; (B) 100 µM Fe(II) treatments; (C) 1000 µM Fe(II) treatments.
945
946
947
948
949

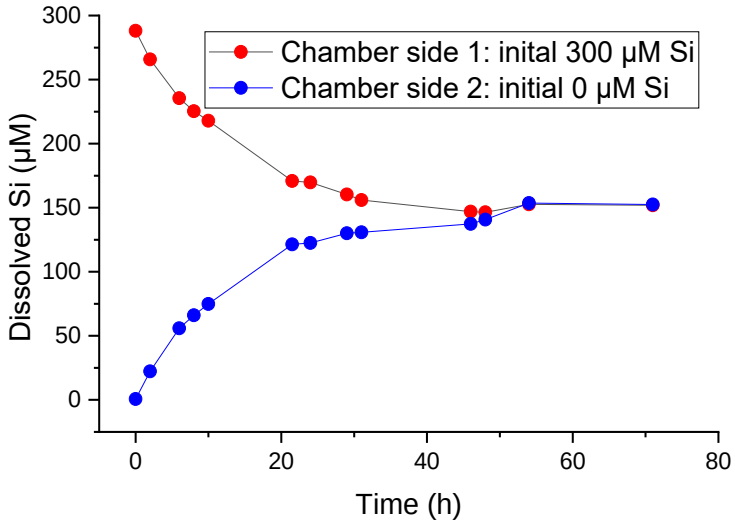

Figure S6. Mixing time for dissolved silica from one chamber to the other across the dialysis membrane of the experimental reactor shown in Figure S1. The mixing time is shown to be < 40 hours.

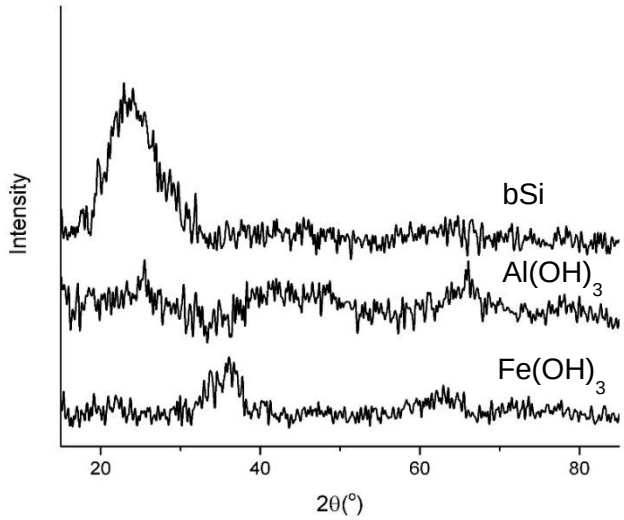

Figure S7. XRD analysis (Cu Kα source) of the initial solid substrates biogenic silica bSi, $Al(OH)_3$, and $Fe(OH)_3$ confirmed all phases were amorphous.

Table S1. Summary of treatment conditions and sample labels without bSi. All treatments contain 150 μM background dissolved silica, $Si(OH)_4$ (DSi). "+" stands for the addition of the reactant.

Treatment group	Dissolved $Si(OH)_4$ (μM)	Dissolved Fe(II) (μM)	bSi	$Fe(OH)_3$	$Al(OH)_3$	Sample label
II (without bSi)	150	0				0Fe(II)+DSi
	150	0		+		0Fe(II)+DSi+Fe
	150	0			+	0Fe(II)+DSi+Al
	150	0		+	+	0Fe(II)+DSi+FeAl
	150	100				100Fe(II)+DSi
	150	100		+		100Fe(II)+DSi+Fe
	150	100			+	100Fe(II)+DSi+Al
	150	100		+	+	100Fe(II)+DSi+FeAl
	150	1000				1000Fe(II)+DSi
	150	1000		+		1000Fe(II)+DSi+Fe
	150	1000			+	1000Fe(II)+DSi+Al
	150	1000		+	+	1000Fe(II)+DSi+FeAl
III (without bSi)	150	100			30 μM dissolved Al^{3+}	Dissolved only

968 **Table S2.** Calculated Si reaction rates from this study.

Reaction condition	Reacted Fe^{2+} (μM)	Authigenic clay Fe/Si ratio	Reaction time	Si reaction rate at experimental condition (μmol/L/month)	Si reaction rate converted to sediments (μmol/cm^3/yr) (porosity = 0.7, density=2.6 g/cm^3)	Si reaction rate (μmol/cm^3/s)
1000 μm dissolved Fe^{2+}, 0.1g /L Al mineral, 0.1g /L $bSiO_2$	500	0.75 (this study)	1 month	667	625.3	19.8×10^{-6}

969

970

971 **Table S3.** Comparison of reverse weathering reaction coefficients reported in literature and from
972 this study.

Location / condition	Reverse weathering reaction rate coefficient (μmol/cm^3/s)	Methods	Estimated global reverse weathering Si sink (T mol/yr)	Refs
Peruvian shelf	3.5×10^{-6}	Model fit dissolved silica and δ30Si data from filed sediments		(*4*)
Sea of Okhotsk	10^{-10} to 10^{-11}	Model fit solutes data from filed sediments		(*5*)
Amazon Delta	1.3×10^{-6}	Estimation of field depth profile annual fluxes of K and authigenic clay K/Si ratio	1.5	(*6*)
Simulates Precambrian marine condition (high Fe^{2+} and Si concentration)	5×10^{-7} to 5×10^{-9}	Polynomial fit of experimental data from Tosca et al., 2016(*7*)		(*2, 7*)
Proximal coastal	3.9×10^{-6}	Model data fitted RW rates matching Si cycle flux from Rahman et al., 2017(*8*)	4.5 − 49	(*9*)
Simulates modern regional high revere weathering rates with sufficient Fe and Al supply in delta environments	19.82×10^{-6}	Zero order rate law extrapolation of experimental data		This study

973

974

975

976

977

978

Table S4. Modern global carbon cycle compiled from Isson et al., 2020 (*1*) and with updated reverse weathering CO_2 source budget.

Source/Sink	Flux (T mol/yr)	References
CO_2 sources		
Metamorphism and volcanism		
Collisional metamorphism	0.5 – 7.0	(*10*, *11*)
Subduction metamorphism	0.3 – ≫1.0	(*12*)
Arc volcanism	1.5 – 3.5	(*13-15*)
Mid-ocean ridge	1.0 – 5.0	(*13-17*)
ocean island	0.12 – 3.0	(*13*, *15*)
Reverse weathering	0.5–10	(*8*, *18*)
CO_2 sinks		
Weathering		
Terrestrial weathering (not including groundwater)	11.5 – 23	(*19*, *20*)
Oceanic crust weathering	0.2—3.75	(*21*)
Marine sediment weathering	5 – 20	(*5*, *22*)
Carbonate precipitation		
Biogenic carbonate	14 – 25	(*22*)
Authigenic carbonate (sediment)	0.5 – 1.5	(*23*)
Authigenic carbonate (oceanic crust)	1.5 – 2.4	(*21*)

References

1. T. T. Isson *et al.*, Evolution of the Global Carbon Cycle and Climate Regulation on Earth. *Global Biogeochemical Cycles* **34**, e2018GB006061 (2020).
2. T. T. Isson, N. J. Planavsky, Reverse weathering as a long-term stabilizer of marine pH and planetary climate. *Nature* **560**, 471-475 (2018).
3. T. T. Isson *et al.*, Marine siliceous ecosystem decline led to sustained anomalous Early Triassic warmth. *Nature Communications* **13**, 3509 (2022).
4. C. Ehlert *et al.*, Stable silicon isotope signatures of marine pore waters - Biogenic opal dissolution versus authigenic clay mineral formation. *Geochimica Et Cosmochimica Acta* **191**, 102-117 (2016).
5. K. Wallmann *et al.*, Silicate weathering in anoxic marine sediments. *Geochimica et Cosmochimica Acta* **72**, 2895-2918 (2008).
6. P. Michalopoulos, R. C. Aller, Early diagenesis of biogenic silica in the Amazon delta: Alteration, authigenic clay formation, and storage. *Geochimica Et Cosmochimica Acta* **68**, 1061-1085 (2004).
7. N. J. Tosca, S. Guggenheim, P. K. Pufahl, An authigenic origin for Precambrian greenalite: Implications for iron formation and the chemistry of ancient seawater. *GSA Bulletin* **128**, 511-530 (2016).
8. S. Rahman, R. C. Aller, J. K. Cochran, The Missing Silica Sink: Revisiting the Marine Sedimentary Si Cycle Using Cosmogenic 32Si. *Global Biogeochemical Cycles* **31**, 1559-1578 (2017).
9. J. Krissansen-Totton, D. C. Catling, A coupled carbon-silicon cycle model over Earth history: Reverse weathering as a possible explanation of a warm mid-Proterozoic climate. *Earth and Planetary Science Letters* **537**, 116181 (2020).
10. J. S. Beckler, N. Kiriazis, C. Rabouille, F. J. Stewart, M. Taillefert, Importance of microbial iron reduction in deep sediments of river-dominated continental-margins. *Marine Chemistry* **178**, 22-34 (2016).
11. E. M. Stewart, J. J. Ague, Infiltration-driven metamorphism, New England, USA: Regional CO2 fluxes and implications for Devonian climate and extinctions. *Earth and Planetary Science Letters* **489**, 123-134 (2018).
12. P. B. Kelemen, C. E. Manning, Reevaluating carbon fluxes in subduction zones, what goes down, mostly comes up. *Proceedings of the National Academy of Sciences* **112**, E3997-E4006 (2015).
13. R. Dasgupta, M. M. Hirschmann, The deep carbon cycle and melting in Earth's interior. *Earth and Planetary Science Letters* **298**, 1-13 (2010).
14. D. R. Hilton, T. P. Fischer, B. Marty, Noble Gases and Volatile Recycling at Subduction Zones. *Reviews in Mineralogy and Geochemistry* **47**, 319-370 (2002).
15. B. Marty, I. N. Tolstikhin, CO2 fluxes from mid-ocean ridges, arcs and plumes. *Chemical Geology* **145**, 233-248 (1998).
16. S. Matthews, O. Shorttle, J. F. Rudge, J. Maclennan, Constraining mantle carbon: CO2-trace element systematics in basalts and the roles of magma mixing and degassing. *Earth and Planetary Science Letters* **480**, 1-14 (2017).
17. A. E. Saal, E. H. Hauri, C. H. Langmuir, M. R. Perfit, Vapour undersaturation in primitive mid-ocean-ridge basalt and the volatile content of Earth's upper mantle. *Nature* **419**, 451-455 (2002).

18. S. Rahman, R. C. Aller, J. K. Cochran, Cosmogenic 32Si as a tracer of biogenic silica burial and diagenesis: Major deltaic sinks in the silica cycle. *Geophysical Research Letters* **43**, 7124-7132 (2016).
19. J. Gaillardet, B. Dupré, P. Louvat, C. J. Allègre, Global silicate weathering and CO2 consumption rates deduced from the chemistry of large rivers. *Chemical Geology* **159**, 3-30 (1999).
20. G. Li, H. Elderfield, Evolution of carbon cycle over the past 100 million years. *Geochimica et Cosmochimica Acta* **103**, 11-25 (2013).
21. L. A. Coogan, K. M. Gillis, Low-Temperature Alteration of the Seafloor: Impacts on Ocean Chemistry. *Annual Review of Earth and Planetary Sciences* **46**, 21-45 (2018).
22. K. Wallmann *et al.*, The Global Inventory of Methane Hydrate in Marine Sediments: A Theoretical Approach. *Energies*. 2012 (10.3390/en5072449).
23. X. Sun, A. V. Turchyn, Significant contribution of authigenic carbonate to marine carbon burial. *Nature Geoscience* **7**, 201-204 (2014).